Palaeoseismic crisis in the Galera Fault (S Spain). Consequences in Bronze Age settlements?

Ivan Martin-Rojas[1], Ivan Medina-Cascales[1], Francisco J. García-Tortosa[2,3], Maria Oliva Rodríguez-Ariza[4], Fernando Molina González[5], José Cámara Serrano[5], Pedro Alfaro[1]

[1] Departamento de Ciencias de la Tierra y del Medio Ambiente, Facultad de Ciencias, Universidad de Alicante, 03080 Alicante, Spain.

[2] Centro de Estudios Avanzados en Ciencias de la Tierra (CEACTierra), Universidad de Jaén, Campus de las Lagunillas s/n, 23071 Jaén, Spain.

[3] Departamento de Geología, Facultad de Ciencias, Universidad de Jaén, Campus Las Lagunillas s/n, 23071 Jaén, Spain.

[4] Instituto Universitario de Investigación en Arqueología Ibérica, Universidad de Jaén, Campus Las Lagunillas s/n, 23071, Jaén, Spain.

[5] Departamento de Prehistoria y Arqueología, Facultad de Filosofía y Letras, Campus Universitario de Cartuja, 18071 Granada, Spain.

Correspondence to: Ivan Martin-Rojas (ivan.martin@ua.es)

Abstract. Palaeoseismological studies play a crucial role in the seismic characterization of regions with slow moving faults. This is the case of the Central Betic Cordillera, a highly populated area where the record of prehistoric earthquakes is very scarce, despite of being one of the regions with the highest seismic hazard in Spain.

We present here a palaeoseismological characterization of the Galera Fault, one of the active faults accommodating deformation in the Central Betic Cordillera. We excavated and analysed several trenches along the fault trace. We quantitatively correlate the results from these trenches, resulting in a surface rupture history involving 7 or 8 events (accounting for the epistemic uncertainties) during the last ca. 24000 yr, with a recurrence interval ranging between 1520 and 1720 yr. Further analysis of this surface rupture history seems to indicate that the Galera Fault is prone to produce earthquakes clusters, as we recorded five events in ca. 400 yr (ca. 1536-1126 BC), and only two events in the next ca. 3200 yr.

Using the fault geometry and palaeoseismological data, we also carried out a seismogenic characterization of the fault. This analysis yielded a maximum expected magnitude of 6.7 ± 0.3 and a recurrence interval of 1857 yr. Furthermore, we also present a geodetic rupture scenario for the maximum expected event, involving displacements of up to 0.5 m.

Finally, we discuss the possible impact of the deduced palaeoearthquakes in the development of Bronze Age human settlements located in the vicinity of the fault. Other than their intrinsic value, our results will be the basis for future seismic hazard assessment carried out in the Central Betic Cordillera.

1 Introduction

The plate boundary between the Iberian Peninsula (Eurasia Plate) and North Africa (Nubia Plate) moves at a moderate rate of

35   5-7 mm/year (DeMets et al., 1994; Nocquet, 2012) (Fig. 1). This plate boundary presents a complex tectonic arrangement, with areas dominated by shortening, extension, and oblique kinematics. Along this boundary lies the Central Betic Cordillera, a region dominated by ENE-WSW extension accommodated mainly by NNW-SSE active normal faults (Fig. 1) (Sanz de Galdeano et al., 2012; Castro et al., 2018; Galindo-Zaldivar et al., 2015; Gil et al., 2017; Martin-Rojas et al., 2023; Medina-Cascales et al., 2020b; Medina-Cascales et al., 2019; Medina-Cascales et al., 2021a; Rodriguez-Fernandez & Sanz de Galdeano,

40   2006; Sanz de Galdeano et al., 2020). Because of this deformation, this region is one of the more active tectonic zones in the Iberian Peninsula and is undergoing significant seismicity (Galindo-Zaldívar et al., 1999; Herraiz et al., 2000; Madarieta-Txurruka et al., 2021a; Madarieta-Txurruka et al., 2022; Morales et al., 1997; Reicherter et al., 2003; Ruano et al., 2004; Sanz de Galdeano et al., 2003). Seismicity in the Central Betic Cordillera includes the most destructive onshore historical earthquake in Spain, the 1884 Andalusian Earthquake (IEMS98 IX-X/estimated magnitude Mw=6.5) (Muñoz & Udías, 1991), and other

45   significant events such as the 1531 Baza earthquake (IMMI VIII-IX; estimated magnitude of ca. 6.0) (Sanz de Galdeano et al., 2012; Martínez-Solares & Mezcua, 2002), the 1964 SW Galera earthquake (mbLg 4.8, VIII) (Martínez-Solares & Mezcua, 2002; García-Tortosa et al., 2007; Silva Barroso et al., 2014) or the 2021 Granada seismic sequence (Lozano et al., 2022; Madarieta-Txurruka et al., 2021b; Madarieta-Txurruka et al., 2022). Moreover, the central sector of the Betic Cordillera has been densely populated since prehistoric times, and today includes important urban centres such as Granada, Guadix, and Baza.

50   Such an intrinsic seismic risk makes seismic hazard assessment (SHA) studies essential in the Central Betic Cordillera. SHAs become increasingly precise as the seismic record is extended further into the past. Therefore, basing an assessment solely on the historic and instrumental record exhibits restricted reliability, especially in areas dominated by slow faults with long recurrence intervals, such as the Betic Cordillera. Thus, the incorporation of palaeoseismological data becomes mandatory to improve the SHA. The problem in this region is that palaeoseismic data are very scarce. The first data were provided by Alfaro

55   *et al.* (2010), who studied liquefaction structures related to the Padul Fault (Fig. 1). They proposed these features as seismic evidence during the Late Pleistocene (ca. 35 to 30 ka). Later, Reicherter *et al.* (2003) conducted a study on the Ventas de Zafarraya Fault (Fig. 1). The authors reported two events in the last 10 ka, prior to the 1884 Andalusian earthquake, and estimated recurrence intervals between 2 and 3 ka for major earthquakes in this fault. The last palaeoseismological study in the Central Betic Cordillera was carried out by Castro *et al.* (2018) in the Baza Fault (Figs. 1 and 2). In this study, they

60   identified 8 to 9 surface-rupturing events in the last 45 ka, providing recurrence intervals of ca. 5 ka. Palaeoliquefaction features were also reported in the Baza and Galera Faults (Alfaro et al., 1997; Alfaro et al., 2010), and were interpreted as indirect evidence of palaeoearthquakes. These pioneering results are essential for seismic hazard assessment studies, but the overall palaeoseismic record of the active faults in the Central Betic Cordillera is still very poor considering that many faults still lack their own studies.

65   The aim of this work is to provide the first palaeoseismic data from the Galera Fault, one of the active structures accommodating present deformation in the Central Betic Cordillera. We provide and describe palaeoseismic evidence from two trench sites. We depict stratigraphic and structural observations on the trench walls and carry out a Bayesian analysis to model the first surface rupturing history for the Galera Fault, including evidence from the two sites. Then, we calculate the recurrence intervals between the proposed events. We also discuss the temporal fault behaviour, in terms of potential temporal

70   clustering. Furthermore, we carry out a preliminary seismogenic characterization of the fault, calculating the main parameters of its seismic potential and modelling a geodetic rupture scenario. Finally, we discuss the implications of our findings in terms of the potential impact of palaeoearthquake clustering on Bronze Age human societies distributed near of this active structure.

2 Geodynamic and geological setting

75

The Galera Fault is located in the Guadix-Baza Basin, in the central sector of the Betic Cordillera (western Mediterranean region) (Fig. 1). Since the late Miocene, the geodynamic setting of the Betic Cordillera has been conditioned by the NNW-SSE convergence between the Nubia and Eurasia Plates (approximately 5–7 mm/year) (DeMets et al., 1994; Nocquet, 2012). Under this background, the Central Betic Cordillera is dominated by a regional NNW-SSE shortening (DeMets et al., 1994;

80   Galindo-Zaldívar et al., 1993; Herraiz et al., 2000; Nocquet, 2012; Sanz de Galdeano & Alfaro, 2004) combined with perpendicular extension with a main ENE-WSW orientation (e.g., (Galindo-Zaldivar et al., 2015; Galindo-Zaldívar et al., 1993) and rates estimated to be between 2.1 and 3.7 mm/yr (e.g., (Pérez-Peña et al., 2010; Serpelloni et al., 2007). Since the Miocene, this extension has been responsible for NNW-SSE, highly dipping normal faults, and SW-NE to W-E oblique faults (e.g., (Alfaro et al., 2008; Sanz de Galdeano et al., 2012; Galindo-Zaldivar et al., 2015; Gil et al., 2017; Martínez-Martínez et al.,

85   2006; Medina-Cascales et al., 2020a; Medina-Cascales et al., 2020b; Medina-Cascales et al., 2021a; Pedrera et al., 2006; Rodriguez-Fernandez & Sanz de Galdeano, 2006; Sanz de Galdeano et al., 2020). In the Guadix-Baza Basin (Fig. 1), the main structures accommodating the regional extension are the normal Baza Fault (Alfaro et al., 2008; Castro et al., 2018; Medina-Cascales et al., 2020b) and the oblique Galera Fault (García-Tortosa et al., 2011; Medina-Cascales et al., 2021b).

The GF is an intrabasinal fault that offsets and juxtaposes rocks of the Guadix-Baza Basin sedimentary infill (Figs. 1 and 2).

90   The basin infill consists of upper Miocene to Quaternary sediments that cover Palaeozoic to Neogene rocks from the Betic Internal and External Zones (García-Aguilar & Martín, 2000; García-Aguilar & Palmqvist, 2011; Gibert et al., 2007; Gibert et al., 2007; Soria et al., 1987; Soria et al., 1999; Vera et al., 1983; Vera, 1970). The Guadix-Baza Basin was established as an endorheic continental basin during the late Miocene after a marine to continental transition due to the regional uplift of the Central Betic Cordillera (Corbí et al., 2012; Sanz de Galdeano & Vera, 1992; García-Aguilar & Martín, 2000; Peña, 1985).

95   From the Early Pliocene to the Middle Pleistocene, the basin was dominated by extensive continental sedimentation (García-

Tortosa et al., 2008; Gibert et al., 2007; Gibert et al., 2007), resulting in the accumulation of more than 2000 m of sediments (e.g., Vera, 1970; Peña, 1985; Vera *et al.*, 1994; Soria *et al.*, 1987). During the endorheic stage, the GF did not develop any surface expression, since the slow vertical slip rate was surpassed by the sedimentation rate, and thus, any geomorphic evidence was easily buried (Medina-Cascales et al., 2021).

100 The Guadix-Baza Basin became exorheic in the Middle Pleistocene (600–500 Ka, Gibert *et al.*, 2007b; García-Tortosa *et al.*, 2008 and 2011) after its drainage was captured (Calvache Quesada & Viseras, 1995; Diaz-Hernandez & Julia, 2006; García-Tortosa et al., 2008; Gibert et al., 2007; Gibert et al., 2007; Scott & Gibert, 2009). Since then, extensive sedimentation ended, and erosion dominated the basin. Deposition of new sediments during recent Quaternary times is restricted to the basin margins (alluvial fans and piedmont deposits) and the modern drainage system (fluvial terraces and valley-bottom deposits). During

105 the exorheic stage, the GF displacement led to the development of certain geomorphic expressions. This expression is reflected mainly by a gentle elevation in its upthrown and a control of the development of the drainage network in the NE sector of the basin (García-Tortosa *et al.*, 2011; Medina-Cascales *et al.,* 2021).

The GF is a SW-NE fault that extends 30 km along the NE sector of the Guadix-Baza Basin (Figs. 1 and 2). The GF presents a slow, oblique displacement, characterized by a main left-lateral (0.5 ± 0.3 mm/yr, Alfaro *et al.*, 2021) and a minor vertical

110 (0.02–0.24 mm/yr, García-Tortosa *et al.*, 2011; Medina-Cascales, 2021) slip component. The GF acts as a transfer structure of the normal Baza Fault, which is located to the SW (Fig. 1) (Alfaro et al., 2021). The surface expression of the GF consists of a fault zone with a width that ranges from a few tens of metre to 1500 m (Fig. 2). The fault zone geometry shows remarkable along-strike variations, changing from extensional duplex structures in the SW to en echelon and linear patterns to the NE, including a pull-apart basin (Fig. 1) (Medina-Cascales *et al.*, 2021).

115 In addition to geodetic (Alfaro *et al.,* 2021) and geomorphic (García-Tortosa *et al.*, 2011; Medina-Cascales *et al.,* 2021) evidence of recent fault activity, the GF presents both palaeoseismological and instrumental associated seismicity. Near the GF fault zone, more than 10 levels of giant seismites can be identified within the Pliocene to Pleistocene sedimentary succession (Alfaro *et al.,* 1997 and 2010), pointing to the occurrence of relatively large magnitude earthquakes in the area. More recently, during instrumental times, the GF was the seismogenic source of the 1964 Galera Earthquake (I= VIII, 4.7

120 mbLg, (Martínez-Solares & Mezcua, 2002). This earthquake was responsible for severe damage to many buildings in Galera, Orce, Huéscar, and Castilléjar villages (Silva Barroso et al., 2014), for partially reactivating a massive rock avalanche close to Galera village, and for causing a great social alarm. The GF has also been proposed as the seismogenic source of the 1973 Huéscar Earthquake (4.0 mbLg) and the background seismicity in the area.
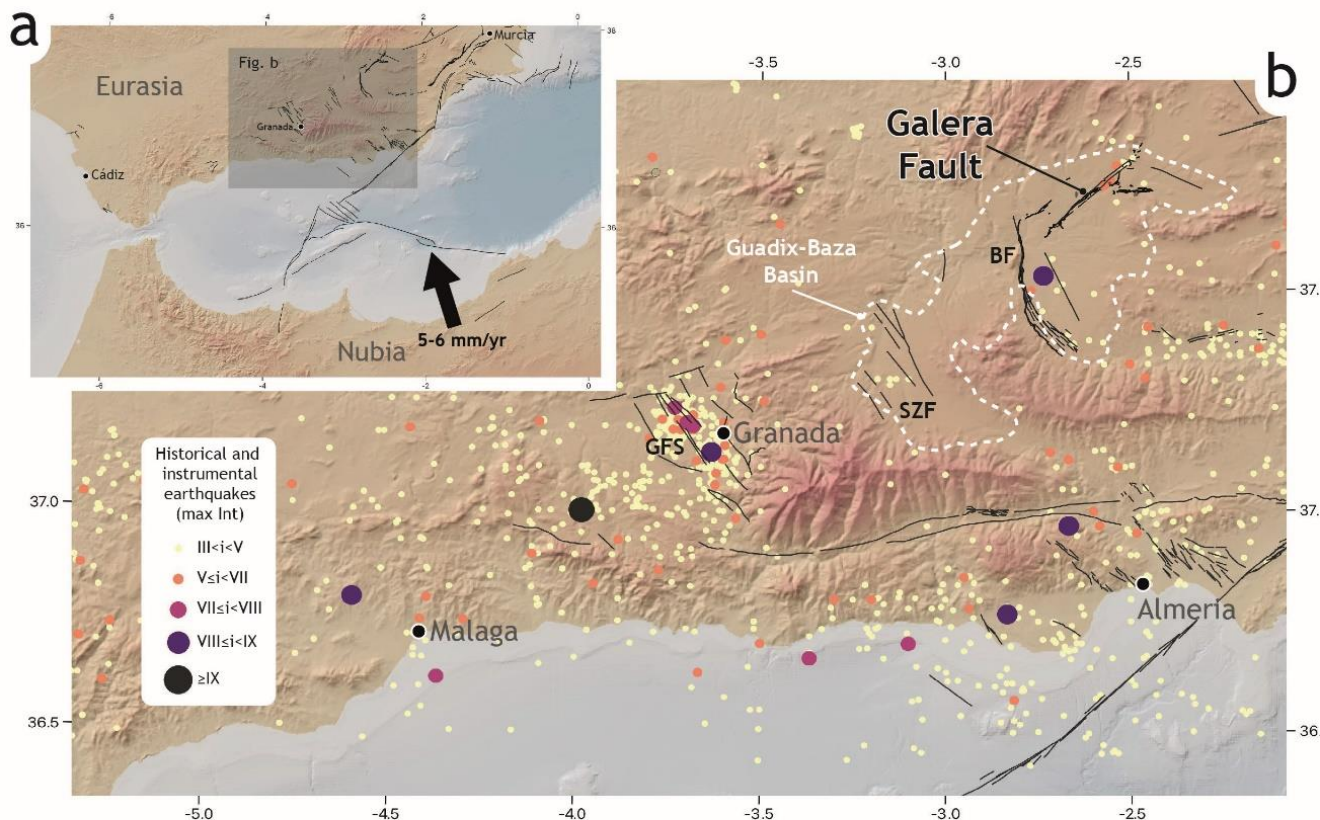
125

Figure 1: a, Tectonic setting of the Western Mediterranean region. b, Seismotectonic map of the Central Betic Cordillera. BF, Baza Fault. SZF, Solana del Zamborino Fault. GFS, Granada Fault System.

2 Results

In this section, we present the main results of the palaeoseismological analysis carried out at two trench sites of the Galera
130 Fault (Fig. 2). This analysis includes a tectonic geomorphological study, a description of the trenches stratigraphy and structure and a surface rupture history deduced for each site.
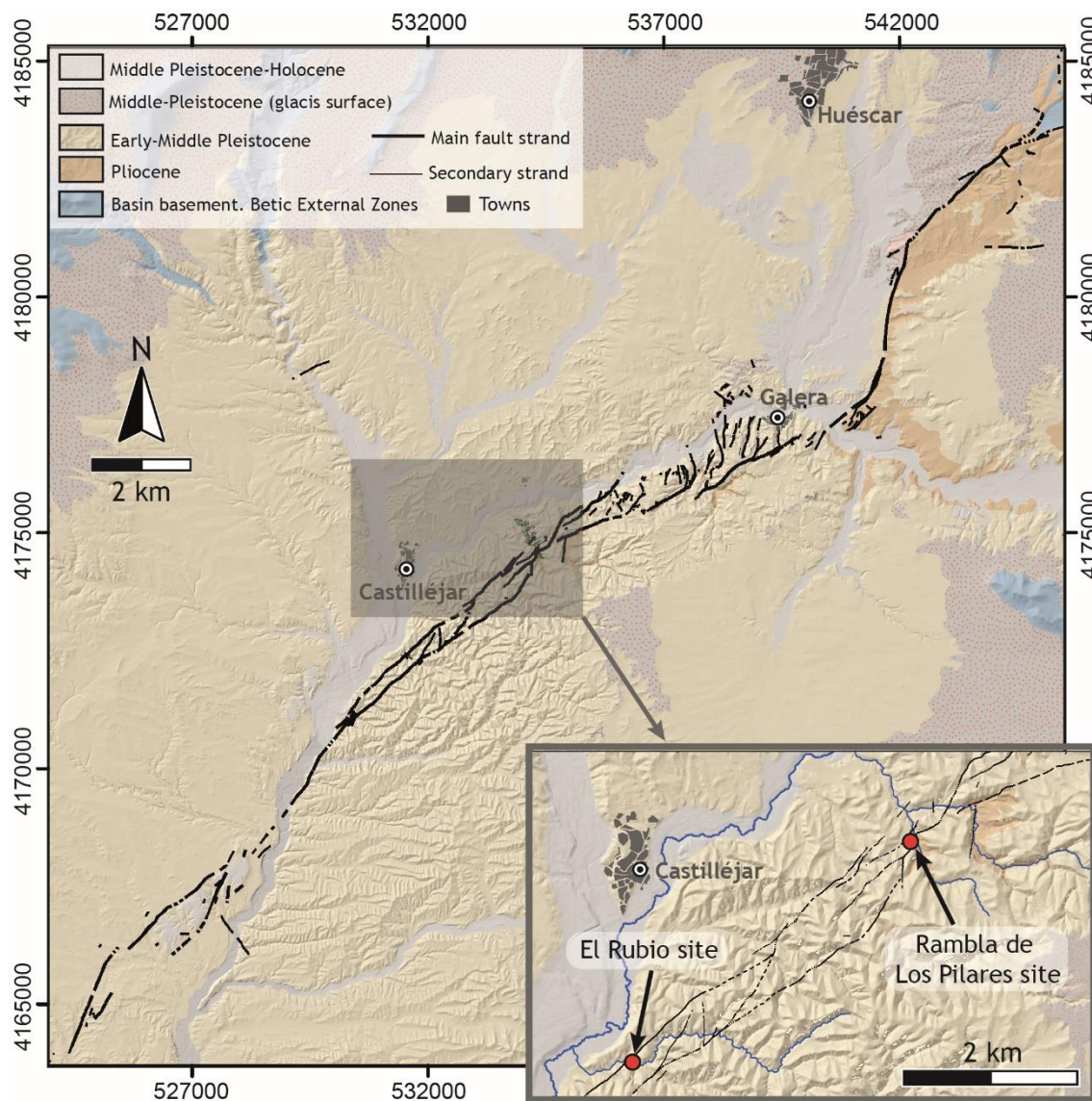
Figure 2: Geological map of the strike-slip Galera Fault. Inset shows the location of the trench sites analized in this
135 **study.**

3.1 Rambla de los Pilares Site

The Rambla de los Pilares site (PIL site; UTM 30S534278/4174615, Fig. 2) is to the east of Castilléjar town. In this area, the
Galera Fault zone reaches 350 m wide and is formed by several N30E to N45E striking fault strands. The palaeoseismological

140 analysis in the PIL site is focused where a N40E, S-dipping secondary strand offsets recent fluvial deposits. In the trench area,

a main gully is downcut into lower Pleistocene sediments (ca. 2.5 Ma, Fig. 3) and flows SES-NWN, roughly perpendicular to the GF. The main geomorphological features of the study area are flat landforms that appear on both sides of the gully. These landforms correspond to a geomorphic surface dissected by the gully, which dips gently towards the N (downstream) and is located ca. 15-20 m above the present thalweg. This surface is the top of a Holocene depositional fluvial terrace that presents

145   variable thickness as it is accommodated to the morphology of the valley, reaching a maximum thickness of ca. 5 m. The fault strand at the PIL site presents a subtle geomorphic expression, although it juxtaposes the fluvial terrace deposits against the Pleistocene deposits. The PIL site consists of 3 parallel trenches (trenches 1, 2, and 3) that were excavated on the western side of the gully, on the fluvial terrace surface and across the secondary fault strand (Fig. 3).
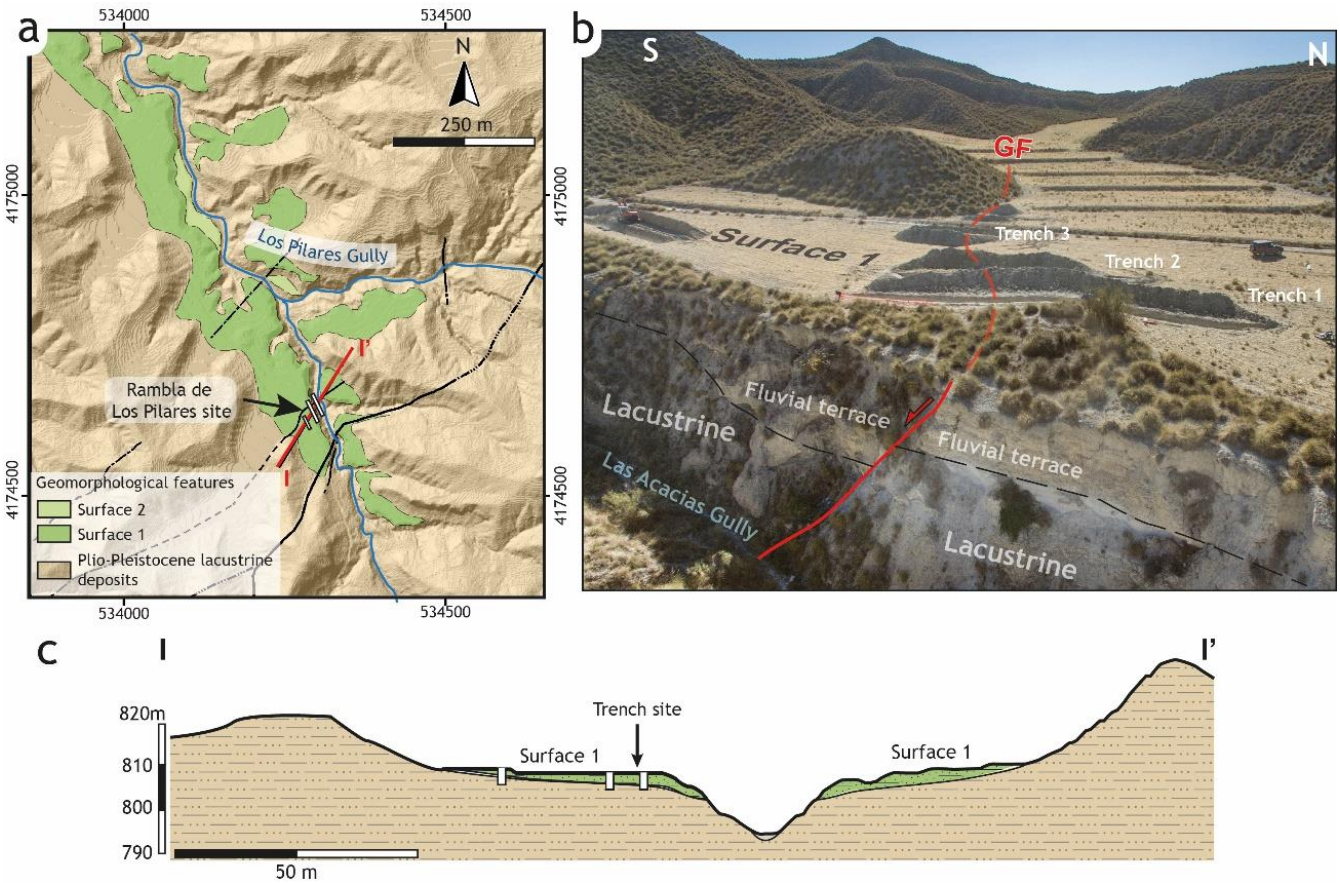
150   **Figure 3: a, Geological/geomorphological map of the Ramblas de los Pilares site. b, Oblique view of the trenching site showing subtle geomorphic imprint of the GF. c. Geological cross section of the trench site.**

3.1.1 Trench stratigraphy

A common stratigraphy is observed in the three excavated trenches (Fig. 4). We group stratigraphic units of the PIL site into

155   bedrock units, fluvial terrace deposits, and modern topsoil.

The bedrock units that we observe in the trench are lower Pleistocene lacustrine deposits. They consist of well-bedded sediments including silts, clays, limestones, and gypsum veins (Fig. 4).
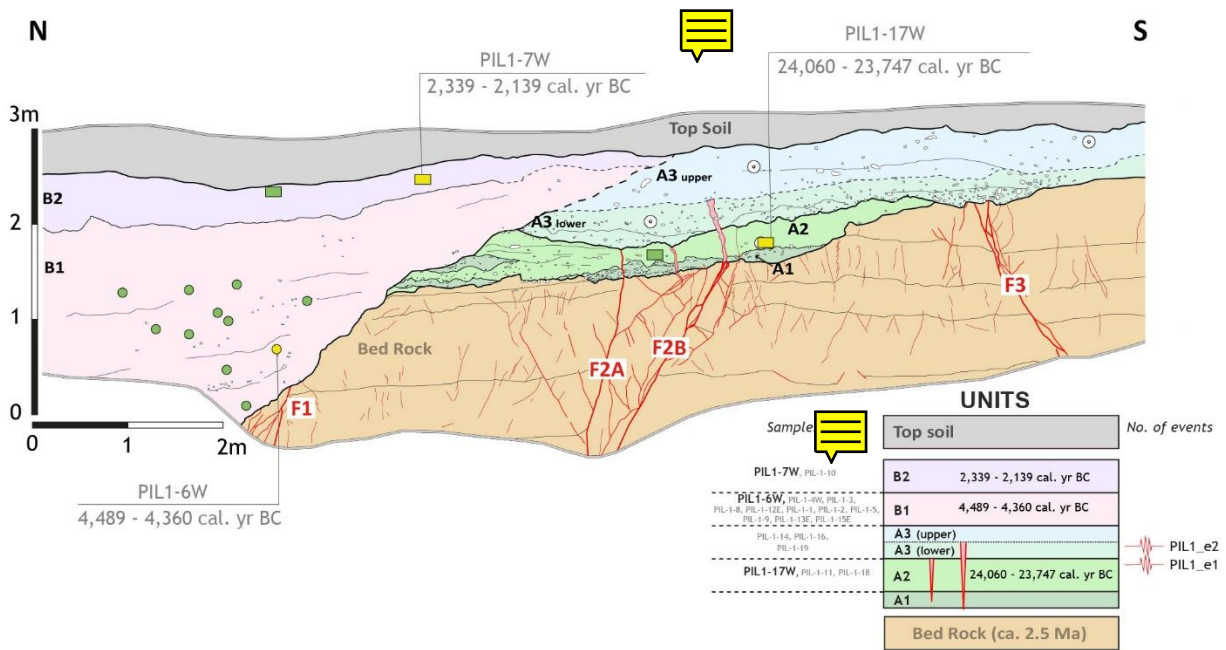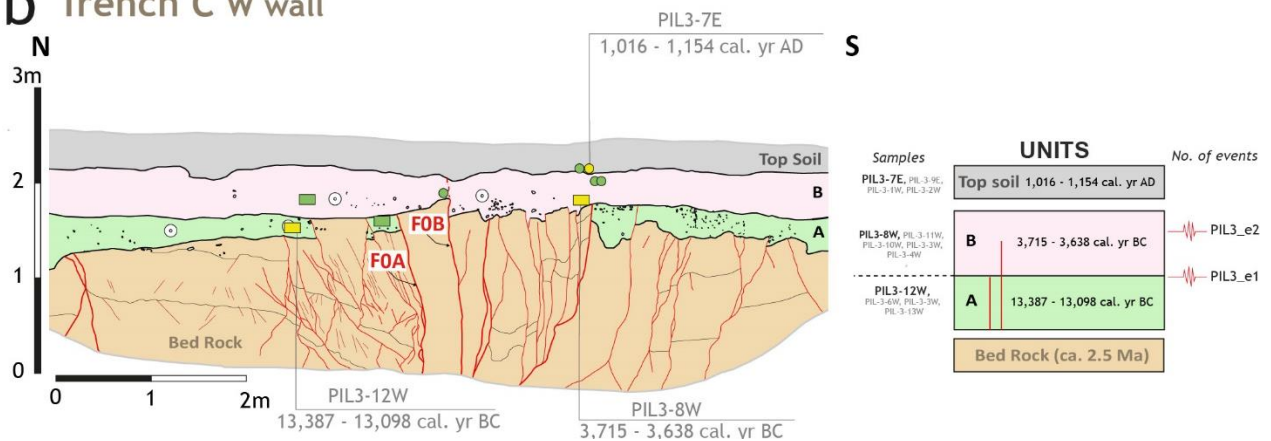
Figure 4: Trench logs and interpretation in terms of palaeoseismic stratigraphic units and events of PIL site. Circles represent charcoal samples (yellow dated, green non-dated). Rectangles, bulk radiocarbon samples (yellow dated, green non-dated). White circles with grey dots, OSL samples.

Fluvial terrace deposits appear unconformably over the bedrock units (Fig. 4). These deposits are disposed in two units: a
165   lower unit A and an upper unit B. In trench 1, three subunits are distinguished within unit A: A1, A2, and A3. A1 overlays the
bedrock and is formed by small channel-shaped bodies with erosive basal contacts. They consist of greyish, massive, matrix-
supported, microconglomerates with irregular gypsum and carbonate clasts and sandy matrix. A2 unconformably overlays A1
and the Pleistocene bedrock. It consists of greenish cemented, fine-grained sands to sandy-silts. A3 overlays A2 and the
bedrock and is made up of greyish, massive, poorly sorted, gypsum-cemented breccia with irregular, cm-sized gypsum and
170   carbonate clasts, and a sandy matrix. In trench 2, unit A is formed only by subunit A3, while in trench 3, unit A is represented
only by subunit A2. Unit B unconformably lies over both unit A and bedrock units (Fig. 4). In trenches 1 and 2, unit B is a ca.
2.5 m thick wedge-shaped deposit that overlaps both bedrock and unit A. We distinguish two subunits within unit B: B1 and
B2. Both subunits are formed by massive brownish silts. B1 is characterized by a dark brown colour, and within it we
distinguish a level of small channel-shaped bodies of microconglomerates and some levels of carbonate pebbles. Moreover, at
175   the bottom of subunit B1, a laterally-continuous level rich in charcoal crops out. We interpret this level as a burn horizon. B2
overlies B1 and is characterized by a light brownish colour and an erosive base. In trench 3, unit B is represented only by a
dm-thick bed of subunit B1.

Finally, overlying all the previously described units, we distinguish a poorly sorted, loose sandy unit with an erosive base that
includes plant roots (Fig. 4). We interpret this unit as a modern topsoil.

180

3.1.2 Trench structure and surface ruptures

Several fault strands are observed in the walls of the excavated trenches (Fig. 4). These fault strands clearly offset bedrock
beds and can be followed across terrace units as they produce a fabric subparallel to fault strands in the conglomerates, which
we interpret as the result of coseismic shearing. Moreover, differential cementation responsible for a higher resistance to
185   erosion is also observed. We use crosscutting relationships as the main evidence to identify palaeoseismic events at the PIL
site. Only trenches PIL1 and PIL2 yield significant palaeoseismic results.

We identify three main faults (F1, F2, and F3) in trench PIL1, as these faults offset bedrock units (Fig. 4). F2 presents the
largest offset and is the only fault crosscutting the terrace units. In this trench, we recognize two palaeoseismic events. A first
event (PIL1_e1) is evidenced by fault strand F2A, which crosscuts unit A2 and is capped by the bottom of unit A3. A second
190   (younger) event (PIL1_e2) is deduced because fault strand F2B intersects the lower part of unit A3 and is capped by the upper
part of this same unit.

We built an OxCal model v4.4.4 (Bronk Ramsey, 2009; Ramsey, 2008; Reimer et al., 2020) that included all the dated samples
to better constrain the ages of the two events recognized in trench PIL1. In this model (Appendix 1), both events were modelled
as a *Date*. Both events have a maximum age limited by bulk radiocarbon sample PIL1-17W (24031-23804BC) collected from
195   the older terrace (unit A2). The minimum age of both events is constrained by detrital charcoal sample PIL1-6W (4494-
4355BC). As the latter was collected in unit B1, belonging to the young terrace, we added a *Zero Boundary* to the OxCal

model, accounting for the time elapsed between the deposition of units A and B. After running the model (Fig. 5), we obtained an age of 24025-17032BC for event PIL1_e1 and an age of 23962-11968BC for event PIL1_e2.

In trench PIL3, the fault zone consists of a central, ca. 0.5 m thick fault core bounded by two main strands (F0A and F0B) that
200 offset the fluvial terrace units. From this fault core, a large number of secondary fault strands branch out, some of which offset the lowermost unit of the terrace. We identified two events in trench PIL3 (Fig. 4). The first event (PIL3_e1) is evidenced by several fault strands (including F0A) crosscutting unit A and being capped by unit B. A second (younger) event (PIL3_e2) is deduced because fault strand F0B offsets the base of unit B and is capped by the bottom of the topsoil.

We also constructed an OxCal model for this trench (Appendix 1). The bulk radiocarbon sample PIL3-12W represents a lower
205 constraint for event PIL3_e1 (modelled as a *Date*). This sample was collected in unit A. The upper constraint for this event is given by sample PIL3-8W. As this latter was collected from the younger terrace, we once again added a *Zero Boundary* to the OxCal model. Event PIL3_e2 (modelled as a *Date*) is constrained between samples PIL3-8W (lower constraint, unit B) and PIL3-7E (upper constraint, topsoil). The upper constraint is located in the topsoil unit; therefore, we also added a *Zero Boundary* to the OxCal model in this position. The OxCal model yielded an age of 13394-8489 BC for event PIL3_e1 and
210 3689 BC-376 AD for PIL3_e2 (Fig. 5).
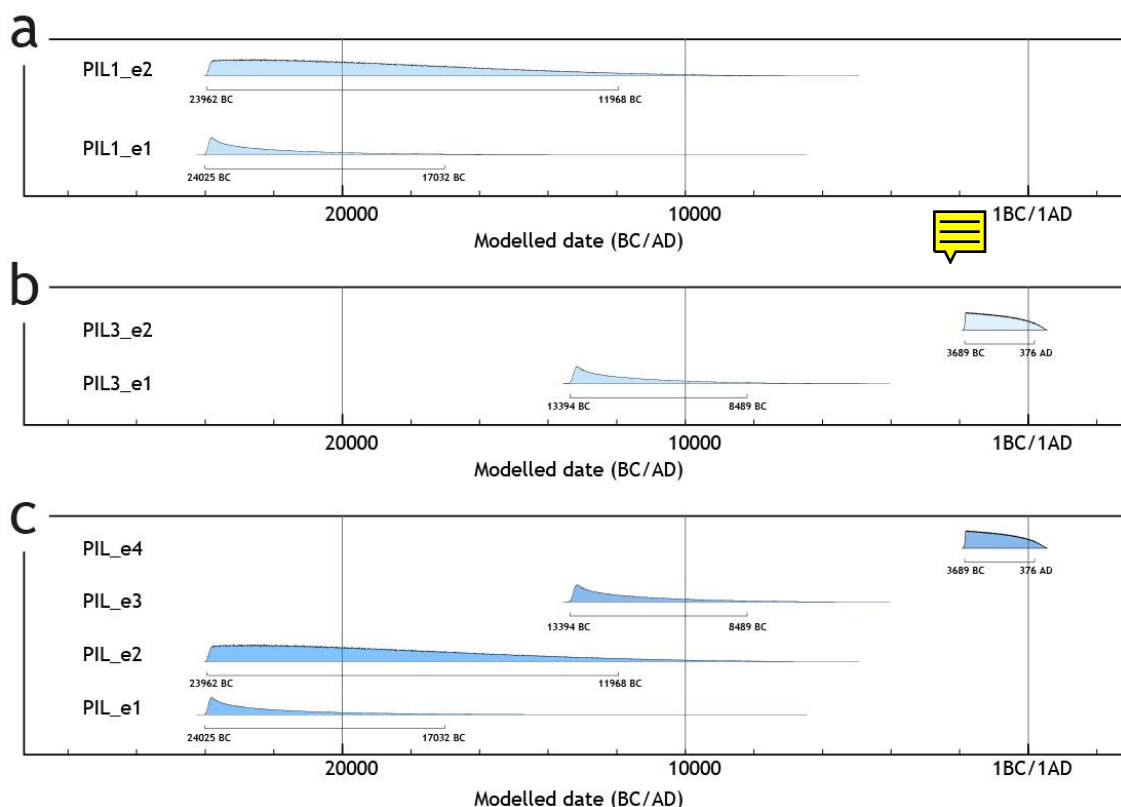
Figure 5: a and b, PDFs from OxCal models for PIL1 and PIL2 trenches, respectively. c, Correlation of PDFs from OxCal models for the PIL site. The low overlap between PDFs indicate that the composite surface rupture for PIL site
215 **comprises four events.**

A visual analysis of the probability density functions (PDFs) of event ages obtained from running the OxCal models shows that event PIL3_e1 partially overlaps with events PIL1_e1 and PIL1_e2. Therefore, these three events could hypothetically be only two events. We quantified the degree of overlap of these PDFs using the methodology proposed by DuRoss et al. (DuRoss
220 et al., 2011). We obtained a very low degree of overlap (0.006 for the pair of PIL3_e1+PIL1_e1 and 0.08 the pair of PIL3_e1+PIL1_e1), so we consider these three events as independent surface ruptures. Therefore, we built a composite surface rupture history for the PIL site involving four events: two registered in trench PIL1 and two in trench PIL3 (Fig. 5c).

3.1.3 Palaeoseismic parameters: Single-event displacement, fault slip rate, and recurrence interval
225 As we already mentioned, fault strands in the PIL1 trench produce differential cementation and a fabric subparallel to the fault in recent deposits. That is, no offset of these recent deposits is observed in this trench. Therefore, we cannot compute single-event displacement or slip rate. In PIL3 trench, the bottom of unit A is vertically offset 0.13 ±0.05 m in the south part of the trench (Fig. 4), which is one of the pieces of evidence of event PIL3_e1. This offset is capped by unit B, indicating that this fracture was not displaced during the following event (PIL3_e2). Thus, the abovementioned 0.13 ±0.05 m offset accumulated
230 in one event (PIL3_e1) and represented the vertical single-event displacement. As the fault strand was not reactivated in the successive PIL3_e2 event, we cannot compute the slip rate from this fracture.

In addition, the bottom of unit B is vertically offset 0.16 ±0.05 m by fault strand F0B (Fig. 4). We identified one event offsetting this marker (PIL3_e2); consequently, we assumed 0.16 ±0.05 m as vertical single-event displacement. Furthermore, accounting for the age obtained for this event after our modelling (3689 BC-376 AD for PIL3_e2), we obtained a vertical slip rate of 0.02-
235 0.13 mm/yr. These values are in good agreement with previously reported geological vertical slip rates of the Galera Fault (0.1-0.2 mm/yr; García-Tortosa et al., 2008, 2011; Sanz de Galdeano et al., 2012). Field data indicate that this strand is an oblique fault, as slickenlines present an orientation of 24/235 (Medina-Cascales et al., 2021). Considering this oblique kinematics and the above discussed parameters, we obtained a single-event displacement of 0.4 ±0.1 m, and a slip rate of 0.05-0.33 mm/yr. These values agree with geodetic slip rates calculated for the Galera Fault (strike-slip rate of 0.5±0.3 mm/yr,
240 Alfaro et al, 2021)

We calculated the recurrence interval for the composite surface rupture history of the PIL site. This composite history involves four events (PIL_e1 to PIL_e4). To compute the recurrence interval, we carried out a Monte Carlo analysis using the PDFs of the four events. We ran 10000 simulations for each pair of events (PIL_e1-PIL_e2, PIL_e2-PIL_e3, and PIL_e3-PIL_e4). Each simulation calculated the difference between two random dates (one from each event involved in the simulation). In this way

245 we obtained 30000 (10000 for each pair of successive events) values representing random elapsed times between events. Our Monte Carlo analysis yielded a recurrence interval of 0-12340 years (95% confidence interval; mode of 10340 years) (Fig. 5).

3.2 Barranco del Rubio Site

The Barranco del Rubio Site (RUB site, UTM 30S534278/4174615, Fig. 2) is located south of Castilléjar village. In this sector,
250 the GF consists of a 270 m wide band bounded by two N45E striking, steeply north dipping fault strands: a southern main strand that juxtaposes 2.5 Ma and ca. 2 Ma lower Pleistocene deposits, and a northern strand with lower vertical displacement that offsets rocks very similar in age (ca.2 Ma). The RUB site is in the northern strand, in a gully that flows ESE-WNW, orthogonal to the fault (Fig. 6). Here, a flat, gently N-dipping landform appears on both sides of the gully. This flat landform is the top of an ca. 10-m-thick Holocene depositional fluvial terrace, located 5 m above the present thalweg. These deposits
255 are intersected by the northern branch of the GF. Where the fault traverses the fluvial terrace, a subtle topographic scarp is observed. This scarp is highly modified due to agricultural activity (Fig. 6). A 12-m-long and 3.5-m-deep trench was excavated on the eastern side of the gully, on the fluvial terrace surface and orthogonal to the GF fault strand (Fig. 6). We describe the south wall of the trench because sun exposition hindered the analysis of the north wall.
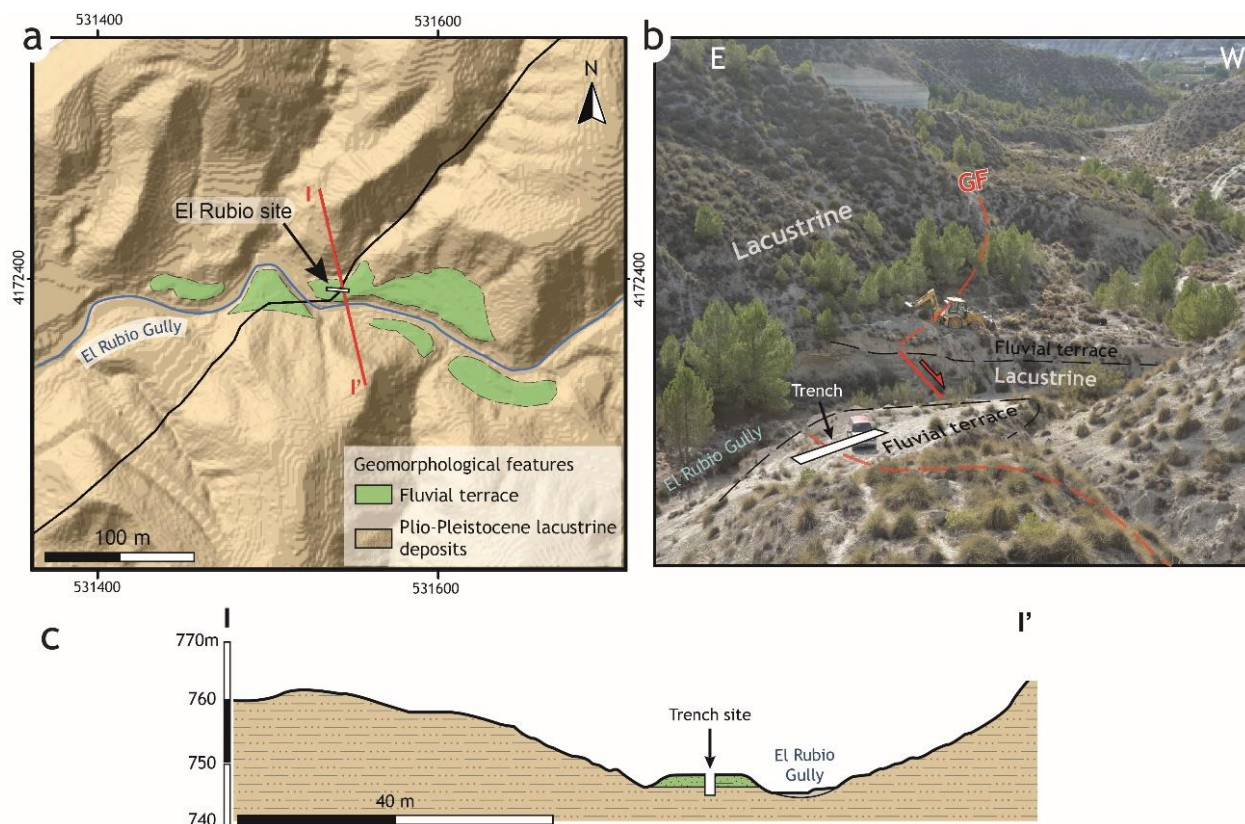
Figure 6. a, Geological/geomorphological map of the El Rubio site. **b,** Oblique view of the trenching site showing the GF crosscutting the fluvial terrace. **c.** Geological cross section of the trench site.

3.2.1 Trench stratigraphy

The RUB trench exposes fluvial terrace deposits that are 3.5 m thick (Fig. 7). These deposits consist of silt and fine sand beds with intercalated levels of fine conglomerates. We differentiated eleven stratigraphic units plus a topsoil level. Unit A, which is 0.25 m thick, consists of centimetric levels of fine sand with intercalations of silts. A 1.5-cm-thick black silt level appears near the base of this unit. Laterally to the west, the uppermost 0.1 m of Unit A is organized in layers 1-2 cm thick consisting of interbedded fine sands and silts with millimetric lamination. This top level within unit A presents a flat bottom and top, but internal layering presents soft-sediment deformation structures (Fig. 8). These structures are mainly sagging load structures, contorted lamination and fluid-escape structures. These soft-sediment deformation structures have been produced by liquefaction and fluidization of the sediment (Owen, 1987). Several processes can trigger sediment deformation, such as overloading or sudden changes in groundwater level (Owen, 1987). In this case, we discard overloading since the studied fine sediments are not related to rapid sedimentation. In addition, soft-sediment deformation structures related to groundwater seepage are morphologically different to those present in the RUB trench. Analogous soft-sediment deformation structures have been described in recent earthquakes (e.g., (Tuttle et al., 2019)) and in analogue models with digital shaking tables (Moretti et al., 1999), and have been widely interpreted as seismites in the geological record also in the Guadix-Baza Basin (Alfaro et al., 1997; Alfaro et al., 2010). Therefore, we interpret the soft-sediment deformation structures present in the RUB trench as result of earthquakes. The general threshold magnitude for sediment liquefaction is around M 5.0, although M 4.5 earthquakes can trigger liquefaction in extremely susceptible soil deposits. Unit B, which is 1 m thick, includes several cm-thick levels of light brown fine deposits and a bed of matrix supported conglomerates. One of the layers within unit B present soft-sediment deformation structures, that we also interpret as seismite (Fig. 8). In the downthrown unit B varies in thickness along-section, as it thins above structurally high parts and thickens in depressed areas. Moreover, dips decrease up-stratigraphy and increase up-dip. Furthermore, levels within unit B present an onlapping geometry. Considering these features, we interpret the geometry of unit B as a growth fold. Unit C, which is 0.75 cm thick, unconformably overlies unit B. Unit C consists of light grey interbedded sands and silts with levels of matrix-supported conglomerates. Conglomerate clasts are rounded and centimetric in size. Clasts consist of carbonates and gypsum, probably derived from the Pleistocene basement. In the downthrown, a 0.15-cm-thick level with soft-sediment deformation structures occurs at the top of Unit C (Fig. 8). Once again, we interpret these structures as seismites. Unit CW1 is formed by clast-supported poorly sorted gravels. Clasts are angular fragments of cemented grey silts and sands, as well as rounded carbonates, probably derived from lower units. This unit is thicker at the fault and thins away from the fault; that is, unit CW1 presents a wedge shape. Accordingly, we propose that unit CW1 is a scarp-derived colluvial wedge. Unit D, which is 0.7 m thick, conformably overlies units C and CW1. Unit D crops out only in the downthrown and is formed by interbedded light brown sands and silts with intercalated matrix-supported conglomerates. Conglomerates are well-cemented, and their clasts are rounded and centimetric in size. Clast lithologies are

carbonates and gypsum. The conglomerate levels present a lens shape, if they are not truncated by the fault. Laterally, internal
295 lamination of the uppermost 0.15 m of unit D are distorted and convoluted (Fig. 8), as a consequence of earthquake-related
shaking. Unit CW2 presents the same features as unit CW1; therefore, we interpret unit CW2 as a second colluvial wedge.
Unit E, which is 0.2 m thick, conformably overlies units D and CW2. Unit E crops out exclusively on the downthrown and
consists of light grey interbedded fine sands and silts. The presence of soft-sediment deformation structures permits us to
interpret this level as a seismite. Unit F, which is 0.45 m thick, crops out in the downthrown and is formed by brownish silts
300 with scarce intercalated levels of very fine sand. Unit CW3 presents the same features as CW1 and CW2, so we also interpret
this unit as a colluvial wedge. Unit G, which is 0.43 m thick and appears in the downthrown, is formed by greenish sandy silts
with no internal structure (massive) and sporadic carbonate and gypsum clasts that are 1-2 cm in size. Unit X, which is 0.65 m
thick, unconformably overlies unit C on the upthrown. This unit consists of slightly cemented conglomerates with centimetric
clasts. These clasts are rounded-carbonate clasts and angular gypsum clasts. Unit Y, which is 0.7 m thick, crops out in the
305 upthrown. This unit is formed by brownish matrix-supported conglomerates with centimetric dispersed clasts. The matrix
consists of light yellowish silts and fine sands. Unit Z crops out only in the upthrown and is 0.6 m thick. Unit Z is composed
of light brown silts and fine sands. The TS Unit, which is up to 0.9 m thick, is a poorly sorted, loose, and massive deposit
including whitish fine sand and silt. This unit presents abundant plant roots. We interpret this unit as modern topsoil.
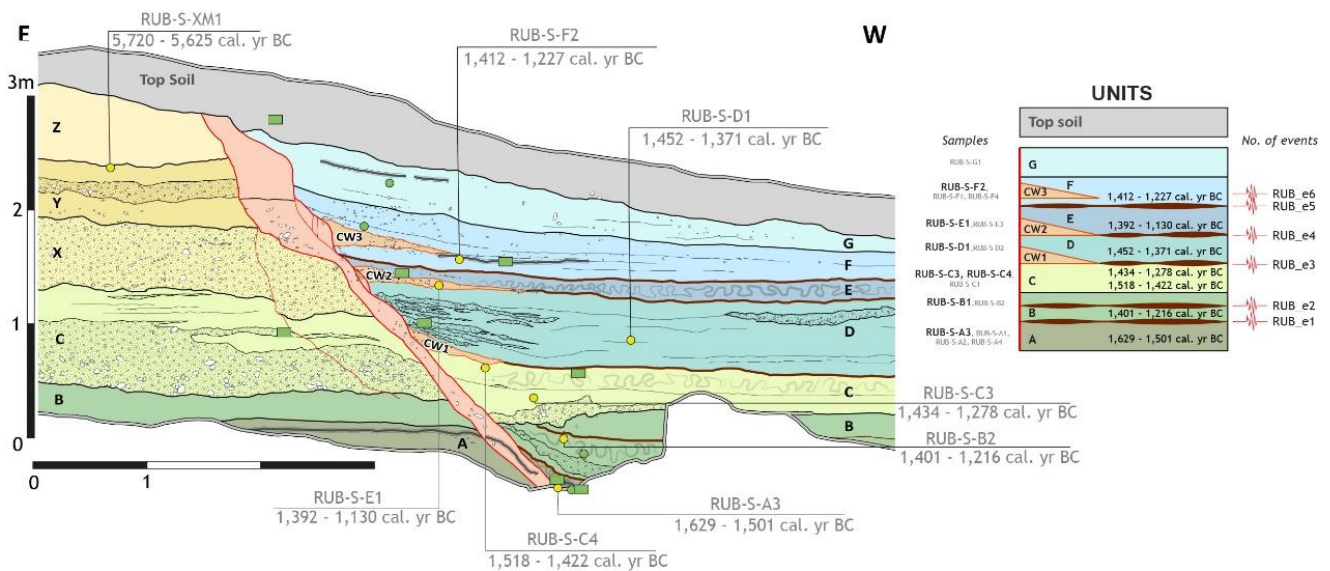
310 **Figure 7. Trench logs and interpretation in terms of palaeoseismic stratigraphic units and events of RUB site. Circles represent
charcoal samples (yellow dated, green non-dated). Rectangles, bulk radiocarbon samples (yellow dated, green non-dated). White
circles with grey dots, OSL samples.**
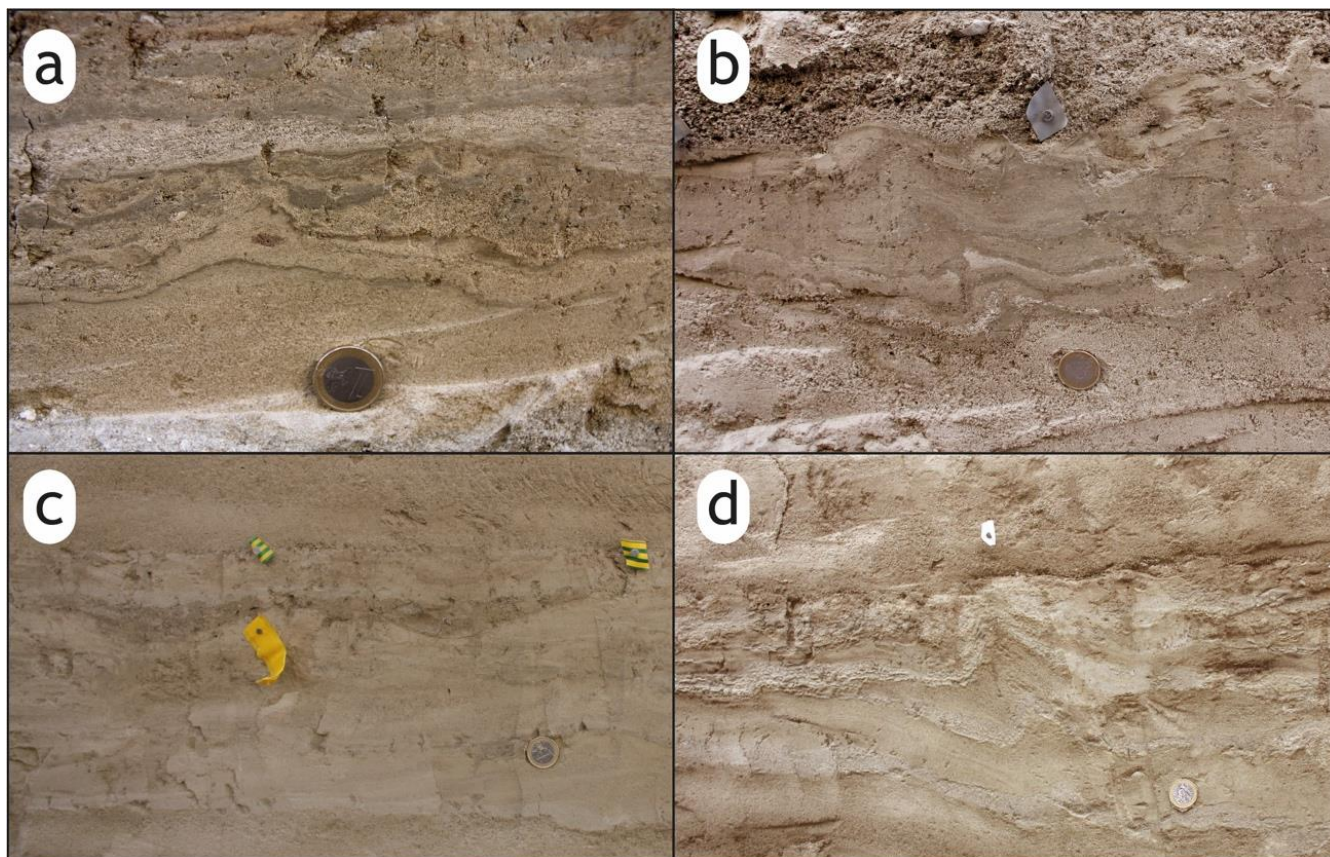
Figure 8. Soft-sediment deformation structures interpreted as seismites in the RUB trench. These structures are mainly sagging load structures (a, unit A; c, unit C), contorted lamination (b, unit B; d, unit D) and fluid-escape structures (a, unit A).

3.2.2 Trench structure and surface ruptures

A fault zone up to 0.5 m thick is observed on the wall of the trench (Fig. 7). This fault zone clearly offsets all the identified units except the topsoil. We use direct and indirect criteria to identify palaeoseismic events at the RUB site, including crosscutting relationships, colluvial wedges, and liquefaction levels. As we already mentioned, we interpret soft-sediment deformation structures observed in the trench as the result of liquefaction induced by earthquakes. Deformed beds remain as separated levels all along the trench (for ca. 12 m). Therefore, we consider each seismite level as an event horizon. However, we cannot completely rule out that all these features had been produced by a single event (Gibert et al., 2011). Liquefaction-related distorted beds are usually formed at the time of deposition and are close to the sediment-water interface (Moretti et al., 1999; Sims, 1975). Therefore, the age of the causative earthquake can be constrained by dating the deformed bed or the levels below and above it. We are aware that liquefaction can occur far from the seismogenic source of the causative earthquake. In the study area, other than the GF, the Baza Fault is also present (Alfaro et al., 2008; García-Tortosa et al., 2011; Medina-

330 Cascales et al., 2020). We cannot completely rule out that the Baza Fault was the source of the events that produced the observed liquefaction structures. However, because of the vicinity to the GF, we assume this latter as the seismogenic source of these events. Distorted beds and convoluted laminations can form at Mercalli intensities of VIII-IX (Green & Bommer, 2019; Sims, 1975; Tuttle et al., 2019). Such intensities can be reached during earthquakes of moderate magnitude, especially when shaking is amplified in sedimentary basins or unconsolidated soils, as is the case at the RUB site. Therefore, although

335 we interpret liquefaction levels as event horizons, the causative earthquakes could have been of moderate magnitude; that is, these earthquakes may or may not have produced surface rupture.

In the RUB trench, we identified seven palaeoseismic events (Fig. 7). The oldest event (RUB_e1) is evidenced by the seismite event horizon at the top of unit A. A minimum age for event RUB_e1 is constrained by deposition of unit B. The second identified event (RUB_e2) is recorded by the seismite event horizon within unit B. Therefore, the minimum age for this event

340 is determined by the deposition of unit C. As they are the only criteria indicating these two older events are liquefaction features, they could have been earthquakes with no surface rupture. The third event (RUB_e3) is recorded by two different criteria: the seismite event horizon located at the top of unit C and colluvial wedge CW1. In this case, the minimum age for this event is constrained by deposition of unit D. Because of the presence of colluvial wedge CW1, we consider RUB_e3 as a surface rupture event. Similarly, event RUB_e4 is evidenced by the seismite event horizon at the top of unit D and colluvial

345 wedge CW2. Therefore, we also consider RUB_e4 as a surface rupture event which minimum age is constrained by the deposition of unit E. Event RUB_e5 is recorded by the seismite level at the top of unit E. Therefore, this would be an event that may or may not have produced a surface rupture and with a minimum age constrained by the deposition of unit F. Event RUB_e6 is evidenced by colluvial wedge CW3. This is a surface rupture event constrained by the deposition of the upper part of unit F. Finally, event RUB_e7 is recorded by the fault strand offsetting up to unit G. This younger event is constrained by

350 the deposition of unit TS.

Two types of palaeoseismic events can be deduced from the RUB trench, as discussed above: events involving surface ruptures (RUB_e3, RUB_e4, RUB_e6, and RUB_e7) and those that may or may not involve surface ruptures (RUB_e1, RUB_e2, and RUB_e5). Therefore, we constructed two OxCal models for the RUB trench. The first model accounts for all the recorded events, while the second model includes only events that have certain surface rupture.

355 The first OxCal model for the RUB site accounts for all the recorded events (Appendix 2) (Fig. 9). In this model, event RUB_e1 (modelled as a *Date*) is constrained by charcoal radiocarbon samples RUB-A3 and RUB-B2 (maximum and minimum constraints, respectively). The OxCal model yields an age range of 1526-1415 BC for event RUB_e1. The same parameters were used in the OxCal model for event RUB_e2. The age of this second event is constrained by sample RUB-B2 (maximum constraint) and charcoal samples RUB-C3 and RUB-C4 (minimum constraints). We obtained an age range of 1491-1411 BC

360 for event RUB_e2. Similarly, event RUB_e3 was also modelled as a *Date*. The maximum constraint for this event is charcoal samples from unit C, as previously mentioned. The minimum constraint is charcoal sample RUB-D1. The model yields an age

range of 1465-1382 BC for event RUB_e3. The next event (RUB_e4) was also modelled as a *Date*. The maximum constraint for this event is charcoal sample RUB-D1. The minimum constraint is charcoal sample RUB-E1, taken from colluvial wedge CW2. We consider that this minimum constraint is closer to the event age, as colluvial wedges are deposited immediately after

365   the earthquake. Therefore, we added a *Zero Boundary* to the model to account for this. The result is an age range of 1440-1322 BC for event RUB_e4. Event RUB_e5 (modelled as a *Date*) is constrained by charcoal samples RUB-E1 and RUB-F2 (maximum and minimum constraints, respectively). The model yields an age range of 1306-1136 BC for event RUB_e5. The maximum constraint for event RUB_e6 (modelled as a *Date*) is sample RUB-F2. However, no dated sample is available above the event horizon of this event. Similarly, no dated samples are available below or above the RUB_e7 event horizon. To better

370   constrain these two events, we added to our OxCal modal a *C_Date* command at 1520 AD. This constraint accounts for the completeness of the Spanish Earthquake Catalogue in the study area (Martínez Solares & Mezcua, 2002). Using these parameters, the model yields an age range of 1029 BC- 099 AD for RUB_e6 and 161 BC-1303 AD for RUB_e7.
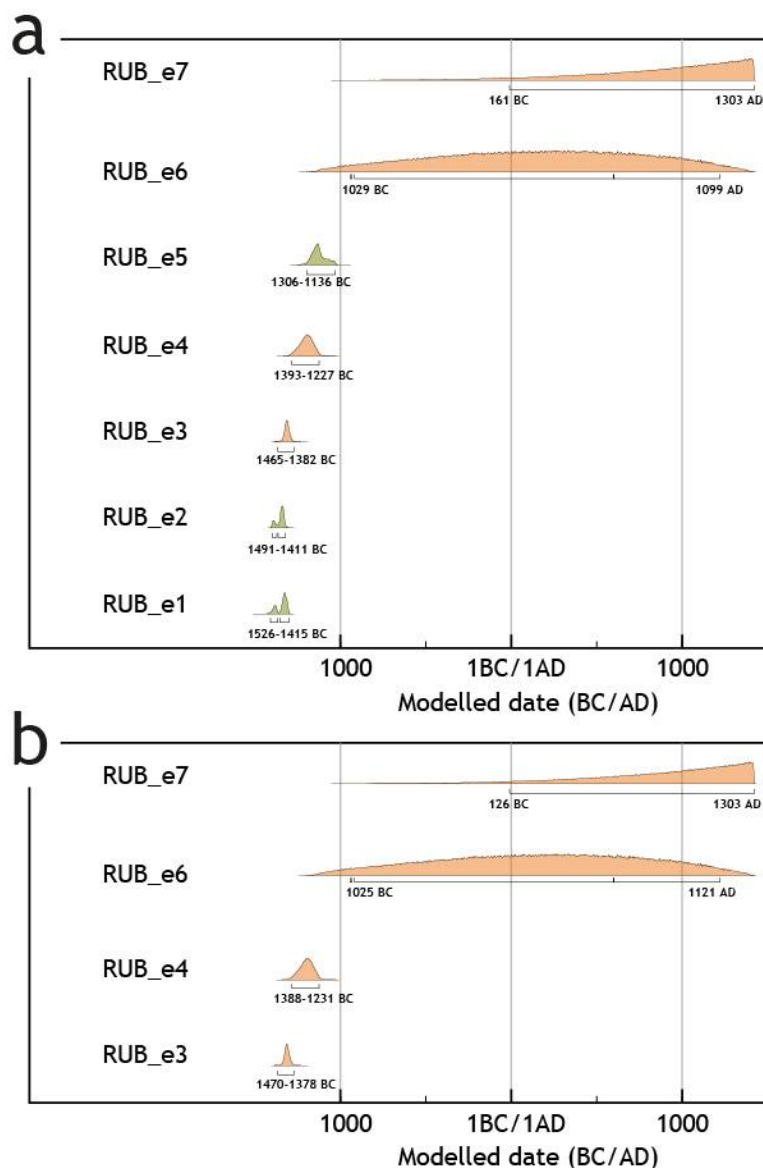
Figure 9. PDFs from OxCal models for RUB trench. a, PDFs accounting for all the recorded events. b, PDFs accounting exclusively
375 **for those earthquakes with certain surface ruptures.**

The second Oxcal model for the RUB site accounts exclusively for those earthquakes with certain surface ruptures, that is,
events RUB_e3, RUB_e4, RUB_e6, and RUB_e7 (Appendix 2) (Fig. 9). This second model is analogous to the first but
eliminhates the *Date* commands related to minor events (RUB_e1, RUB_e2, and RUB_e5). This model yields the following
380 ages: 1470-1378 BC for event RUB_e3, 1388-1231 BC for event RUB_e4, 1051 BC-1121 AD for event RUB_e6, and 126
BC-1303 AD for event RUB_e7.

3.2.3 Palaeoseismic parameters: Single event displacement, fault slip rate, and recurrence interval

Only the three lowermost units (unit A, unit B, and unit C) are recognized on both sides of the fault zone in the RUB trench
385   (Fig. 7). To compute the single-event displacement, we use the black silt level near the base of unit A and the top of the basal
conglomerates of unit C. We selected these two horizons as they can be traced continuously from the upthrown to the
downthrown across the fault zone (Fig. 7). The lowermost correlated level (black silt level near the base of unit A) should have
accumulated the offsets of all the recognized events. The second correlated level (top of conglomerates at the base of unit C)
is located below the event horizon of RUB_e3 (i.e., below the top of unit C). Therefore, this second level should accumulate
390   the offsets of all the events, except RUB_e2 and RUB_e1. However, the along-dip offset measured for both levels is the same
(0.79±0.07 m for the lower level and 0.79±0.06 m for the upper level). We consider that this is evidence that events deduced
only from liquefaction levels were of moderate magnitude and did not produce surface ruptures.

The exposed trench wall shows a normal apparent displacement of this fault strand. However, once again, field data indicate
that this strand is an oblique fault, as slickenlines present an orientation of 24/235 (Medina-Cascales et al., 2021). Considering
395   this oblique kinematics and the above discussed normal offset, we calculated a total offset of 1.64 ±0.11 m. Dividing this value
between the number of events with certain surface ruptures (4), we obtained a mean single-event displacement of 0.41 ±0.11
m.

Using this same dataset and an analogous approach, we calculated the fault slip rate. For this calculation, we assumed that the
total offset observed in the trench is the result of the cumulative displacement of all the recorded palaeoseismic events. Under
400   this assumption, we divided the 0.79 ±0.06 m of the mean normal offset measured between the age of the older event and the
surface rupture recorded in the trench (1470 -1378 BC, event RUB_e3). We obtained a normal (dip) slip rate of 0.23 ±0.07
mm/yr, a strike-slip rate of 0.27 ±0.07 mm/yr, and a total slip rate of 0.49 ±0.07 mm/yr. These values agree with geodetic slip
rates calculated for the Galera Fault (strike-slip rate of 0.5 ±0.3 mm/yr, Alfaro et al, 2021)

We calculated the recurrence interval for the RUB site following the same procedure used for the PIL site. In this case, we
405   carried out three Monte Carlo analyses using the PDFs of the palaeoseismic events Fig. 9): the first analysis includes all the
recorded events, the second analysis includes only those earthquakes with certain surface ruptures, and the third analysis
includes events RUB_e1 to RUB_e5, that is, events that took place in a concentrated period of time (see below). After running
the Monte Carlo simulations including all the events recorded in the RUB trench, we obtained a recurrence interval of 90 years
(0-1790 years at a 95% confidence interval). The second analysis yielded a mean recurrence interval of 575 years (0-2055
410   years at a 95% confidence interval) for events with certain surface ruptures. The third analysis indicated a mean recurrence
interval of 50 years (0-155 years at a 95% confidence interval) for events RUB_e1 to RUB_e5.

4 Discussion

4.1 Composite surface rupture history of the Galera Fault

415

In this section, we discuss the composite surface rupture history of the GF for the last ca. 14000 yrs. We assumed that, because the Galera Fault is not divided into segments and is 30 km long, surface rupture events are fault-wide earthquakes. Therefore, the proposed composite history involves events from both palaeoseismological sites, i.e., PIL and RUB.

As discussed above, we distinguished two different event types at the RUB site (Fig. 8): events with certain surface ruptures

420   and events that may or may not produce surface ruptures. Therefore, to minimize uncertainties, we included in this composite history only RUB events with certain surface ruptures.

Event age PDFs of PIL and RUB trenches are highly heterogeneous. In PIL trench, the ages of each single event obtained after our Bayesian analysis extend up to ca. 10000 yr (Fig. 5). In contrast, events ages in the RUB trench are much better constrained, some of them extending ca. 100 yr (Fig. 9). To encompass this heterogeneity in a composite surface rupture history of the GF,

425   we preferred to integrate our data in a logic tree rather than consider the PDFs overlap of each event (DuRoss et al., 2011, Castro et al., 2018) (Fig. 10).
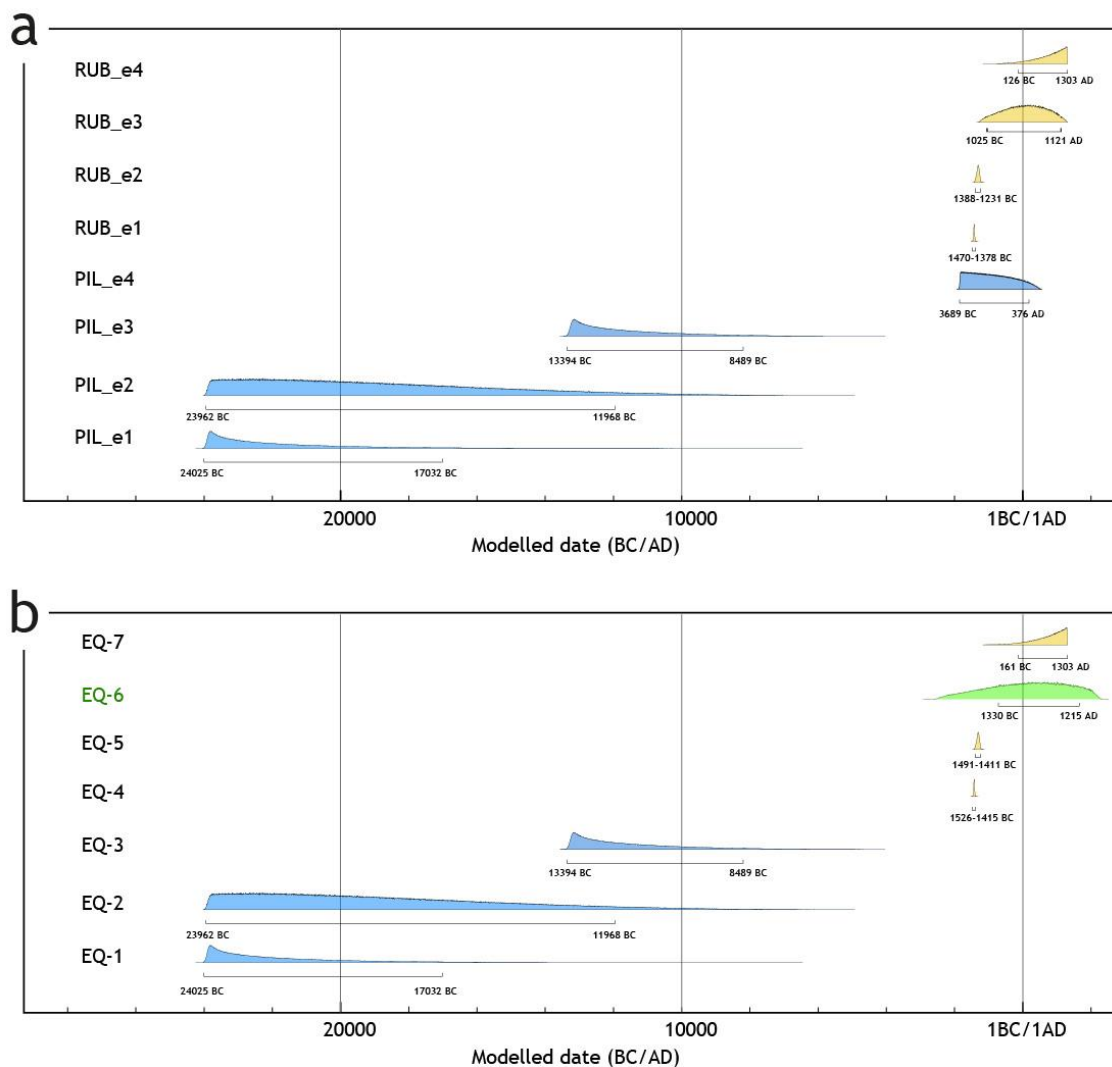
Fig 10. Correlation of PDFs from OxCal models for the GF. a, in the first scenario, PIL_e4 is considered a different event that is not registered in the RUB trench, leading to surface rupture history for the GF involving 8 events. b, the second scenario considers that PIL_e4 is one of the events recorded in the RUB trench, yielding a total of 7 events.

Our logic tree considers two main scenarios (Fig. 10): in the first scenario, PIL_e4 is a different event that is not registered in the RUB trench. In that case, we obtain a composite surface rupture history for the GF involving 8 events for the last ca. 24000 yr. Alternatively, our second scenario considers that PIL_e4 is one of the events recorded in the RUB trench. This second scenario implies a total of 7 events for the last ca. 24000 yr in the GF. As PIL_e4 is poorly constrained, it overlaps all the events recorded in the RUB trench, leading to an additional four branches in our logic tree. This fact, together with the heterogeneous PDFs of both trenches mentioned above, led us to compute composite ages of all the possible combinations under the second scenario (i.e., composite event involving PIL_e4+RUB_e1, PIL_e4+RUB_e2, PIL_e4+Rube3, or

440   PIL_e4+RUB_e4) rather than only that with the highest overlap. However, because events from the RUB trench are much better constrained, the resulting composite ages are in all cases almost the same as those of the original RUB events (varying only ca. 20-40 yr). That is, all the possibilities branching out from our second scenario yield almost identical results. Therefore, here we present only the result of the branch with the highest overlap (composite event PIL_e4+RUB_e3; Fig. 10), but we would like to emphasize that almost identical conclusions are obtained from the other branches.

445   In the first scenario (no common event between the PIL and RUB trenches; a total of 8 events), we obtained a mean recurrence interval of 1520 years (0-2170 years at a 95% confidence interval). In the second scenario (one common event between sites; a total of 7 events), the mean recurrence interval obtained is 1720 years (0-2485 years for 50% confidence interval, 0-12045 years at a 95% confidence interval).

4.2 Temporal distribution of the Galera Fault earthquakes

450

In this section, we discuss the hypothesis of temporal palaeoearthquakes clustering in the GF. Historical and instrumental observations indicate that strike-slip faults commonly present short high-frequency seismic periods alternating with long periods with a lower earthquake rate (Barka, 1996; Chéry et al., 2001; Klinger et al., 2005; Marco et al., 2005; Rockwell et al., 2015). These observations seem to indicate that strike-slip faults are prone to temporal clustering of earthquakes. The lack of

455   sufficiently long consistent earthquake histories usually hampers the testing of this hypothesis in palaeoseismic records.
Data from the RUB trench indicate a short period of ca. 400 years (ca. 1536-1126 BC) when the GF produced five events with a mean recurrence interval of 50 years (0-155 years at a 95% confidence interval, Fig. 9). Two of these events are certain surface ruptures, while the other three probably did not produce surface ruptures. Evidence for these three last events are liquefaction features; therefore, we postulate a minimum threshold of a magnitude 4.5 for them (Green & Bommer, 2019;

460   Moretti et al., 1999). In the next ca. 3200 years, only two events were recorded, although the sedimentary conditions remained analogous. Therefore, these data seem to indicate that the GF might present a behavior characterized by temporal clustering. Such a behaviour should be addressed in future seismic hazard assessments.

4.3 Seismogenic characterization of the Galera Fault

465   In this section we evaluate the seismic potential of the GF by determining its maximum expected magnitude and mean recurrence times between maximum events. Additionally, we simulate a geodetic rupture scenario, providing insights into the fault's behaviour.

4.3.1 Seismic hazard parameters: maximum expected magnitude and mean recurrence times

470   To calculate the seismic hazard parameters of the GF, we utilized the FiSH (Fault into Seismic Hazard) code (Pace et al., 2016). This code is designed for Probabilistic Seismic Hazard Assessment (PSHA) and models faults as seismogenic sources. We computed two key parameters, namely, the maximum magnitude (Mmax) and recurrence time between Mmax events, along with their associated uncertainties.

FiSH incorporates various approaches and scale relationships (Leonard, 2010; Wells & Coppersmith, 1994) to determine the
475   Mmax that the fault can accommodate. These values, along with their uncertainties, are fitted into a global normal distribution, generating mean values and standard deviations for Mmax. Input parameters for FiSH include the fault's total length, mean dip, seismogenic depth, and, if available, the maximum recorded event (Table I).

For the GF, we determined the fault length and dip based on structural data obtained from previous studies (Medina-Cascales *et al.*, 2021). We set the seismogenic depth to 15 km, considering earthquake depths recorded in the area from the Spanish
480   IGN seismic catalogue (Martínez-Solares & Mezcua, 2002) and following criteria used by other researchers in the region (e.g., Galindo-Zaldivar *et al.*, 1997). The maximum recorded event, the 1964 Galera Earthquake presents a magnitude of 4.7 mbLg. This value significantly deviates from the expected maximum magnitude for the fault. FiSH requires an input value close to the maximum magnitude that was ever generated by the fault, which represents its characteristic earthquake. A value of 4.7 is inappropriate because it lowers the mean when averaged with other maximum earthquakes calculated using different
485   approaches. This may result in an unrealistically shorter recurrence period for large earthquakes. Therefore, we did not use the maximum recorded event as an input parameter in our calculations. The estimated maximum expected magnitude (Mmax) remains consistent regardless of the scale relationship that is used, yielding Mw 6.7±0.3 (Table I).

Additionally, we computed the mean recurrence time between Mmax events. FiSH calculates this value by determining the seismic moment for an Mmax event and comparing it to the known slip rate, thereby determining the released moment rate. In
490   this context, the Mmax event is considered a characteristic event that is expected to occur within a specific recurrence interval. The slip rate on the GF, obtained from geodetic data, is 0.5 ±0.3 mm/year (Alfaro *et al.*, 2021) (Table I). Based on the calculated Mmax values that we obtained from the Wells and Coppersmith (1994) and Leonard (2010) scale relationships, the estimated recurrence time between Mmax events on the GF is ca. 1857 years in both cases, with a coefficient of variation of 1.2 (Table I). These values align with the recurrence times calculated through Monte Carlo analysis using palaeoseismological data from
495   the two studied trenches.

Table I. Input parameters and results of the seismic parameters obtained applying the FiSH code (Pace et al., 2016).

Input parameters	
Fault data	
Fault length:	32.5 km
Mean fault dip:	74 °

Seismogenic Depth:		15 km	
Slip-rates	Min:	0.2 mm/yr	
(geodetic)	Max:	0.8 mm/yr	
Seismic Hazard Parameters of the Galera Fault			
Mmax:	Wells and Coppersmith (1994)	6.7 ± 0.3	
	Leonard (2010)		
Recurrence time (Mmax):	Wells and Coppersmith (1994)	1857 years	CV:
	Leonard (2010)		1.2

4.3.2 Permanent displacements caused by an Mmax event

500   After estimating the magnitude of the Mmax earthquake, we proceeded to simulate a geodetic scenario for this event by calculating the permanent displacement caused by the earthquake. This simulation relied on the fault geometry and involved modelling the displacement between the two blocks along the fault slip surface. To evaluate this scenario, we used the Coulomb 3.3 code (Toda et al., 2011), which applies Okada's approach (Okada, 1985; Okada, 1992) to simulate the deformation of an elastic half-space with constant elastic properties.

505   Using the fault geometry (total length, dip, and seismogenic depth), we modelled the Mmax magnitude by assuming a uniform displacement of 0.77 m between the blocks. This corresponds to a seismic moment of approximately 1.24×10^{26} dyn·cm, equivalent to an Mw 6.7 event according to Wells and Coppersmith (1994). The simulation showed a westwards movement of the NW fault block and an eastwards movement of the SE fault block.

    The results are illustrated in Figure 11, showcasing the deformation field and highlighting the horizontal displacements. These
510   displacements reveal the extensive area affected by the maximum expected earthquake from a geodetic perspective. The NW fault block exhibited westwards permanent displacements ranging from 0.40 m to 0.50 m. In contrast, the SE fault block experienced lower eastwards permanent displacements (0.3 m to 0.4 m) near the fault trace. An area with maximum displacement was observed in the NW block, close to the Galera town. Surprisingly, this highly affected area is not located in the central sector of the fault, which we initially assumed would experience the largest displacement. Therefore, we attribute
515   this highly affected area to a main irregularity in the fault trace, specifically a fault bend. The curvature of this fault bend generates regions of maximum displacement, a phenomenon previously observed in the neighbouring Baza Fault (Medina-Cascales *et al.,* 2020).
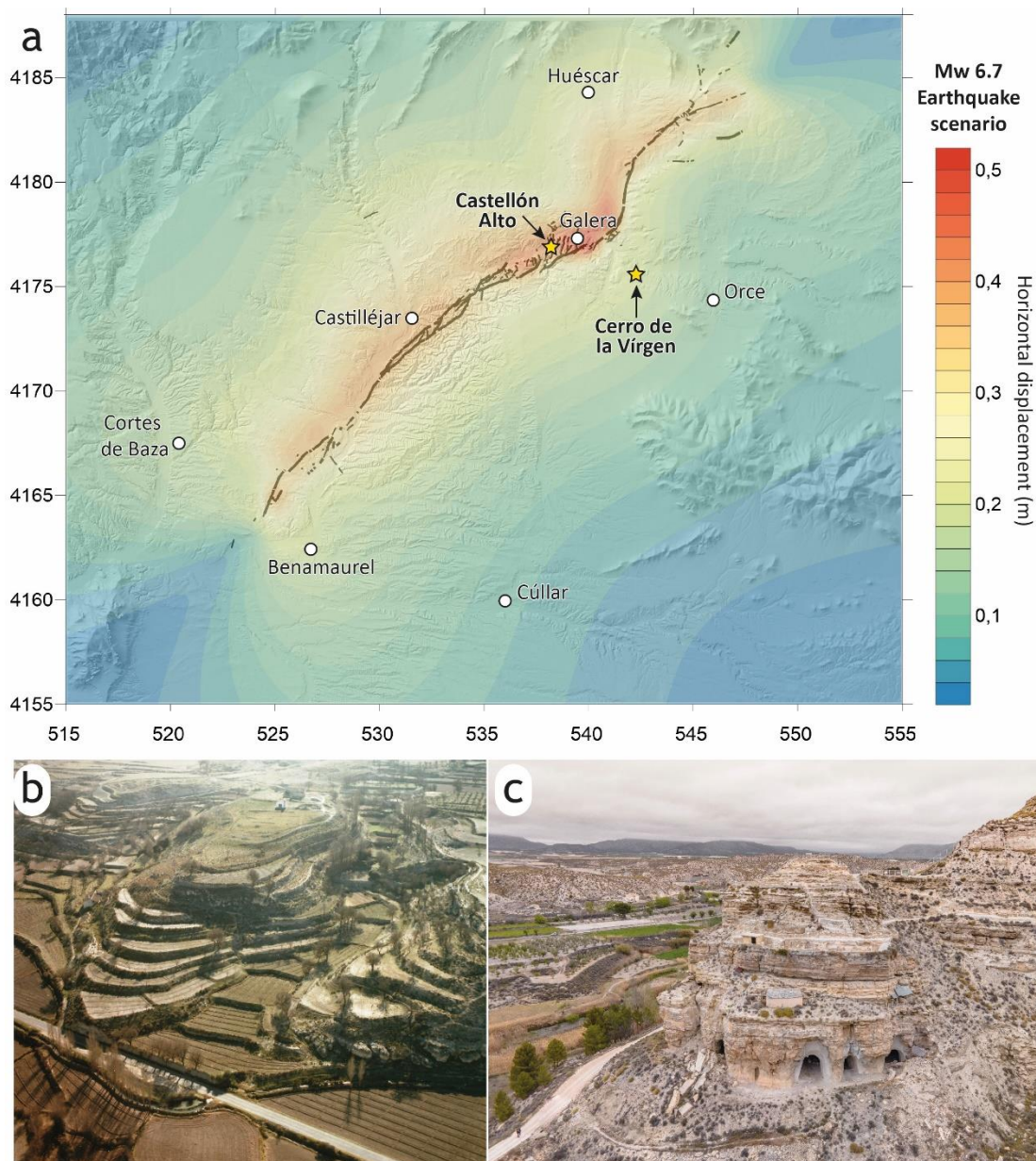
Figure 11. a, Modelled geodetic scenario for the GF expected Mmax earthquake (Mw 6.7). Coloured contours represent amount of horizontal displacement. Stars show the location of Bronze Age human settlements. b and c, Aerial views of the Cerro de la Virgen and Castellon Alto Bronze Age settlements, respectively.

4.3. Implications for Bronze Age human settlements

Natural disasters have traditionally been proposed as important agents in past collapses, destructions or major changes in
525 human societies (Force, 2017; Mastrolorenzo et al., 2006; Oswald et al., 2021; Von Suchodoletz et al., 2022a; Walker et al., 2020). In this section, we discuss our palaeoseismic results in terms of the role that earthquakes could have played in the development of Bronze Age settlements near the GF.

As discussed above, data from the RUB trench indicate a temporal clustering of earthquakes between ca. 1536 BC and 1126 BC. In these ca. 400 years, the GF was responsible for five events, two of them with surface ruptures. This time span
530 corresponds with the Bronze Age historic period. During this period, the Argaric Culture developed in SE Spain, characterized by its ceramic techniques and sophisticated pottery (Castro, 2001). The Argaric Culture flourished in 2200 BC and was active untill 1300 BC (Aranda & Molina, 2006; Hernández Pérez et al., 2016; Molina González, 1978; Schubart et al., 2000).

Two major Argaric archaeological sites are near the GF (Fig. 11): the Castellón Alto and the Cerro de la Virgen sites. The Castellón Alto site (Molina & Cámara, 2004) is located very close to the GF trace (Fig. 11) and is in a steep hill facing a small
535 ravine. This 170x80 m site is divided into four distinct areas and distinguished by narrow streets lined with multiroom stone houses. Most of the burials in the Castellón Alto site consist of small lateral chambers at the bases of vertical pits under house floors or behind house (Cámara & Molina, 2011; Cámara et al., 2018; Molina, 1983). The Castellón Alto settlement had been inhabited since 1900 BC and was abandoned in approximately 1500 BC, as indicated by the more recent tombs (dated to 1600 BC). The Cerro de la Virgen site (Molina González, Fernando et al., 2016) is also located in a steep area, at the confluence of
540 two small ravines (Fig. 11). Three different phases are recognized in this 375x160 m fortified settlement (Molina et al., 2018; Molina et al., 2017; Schüle, 1980). The third phase presents distinct features of Argaric Culture (Molina et al., 2014; Molina et al., 2016; Molina et al., 2018), including burials under house floors or behind house walls. The more recent tombs in the Cerro de la Virgen site are dated to 1550 BC, indicating that the site was abandoned in approximately 1500 BC (Molina et al., 2014; Molina et al., 2016; Castro et al., 2009).

545 The end of the Argaric Culture in SE Spain took place at ca. 1300 BC because of a crisis probably related to its forms of social exploitation (Cámara & Molina, 2009; Lull et al., 2013; Risch & Meller, 2015). However, the two Bronze Era archaeological sites near the GF (Castellon Alto and Cerro de la Virgen) represent an anomaly, as both were abandoned in approximately 1500 BC, i.e., ca. 200 years before other Argaric settlements in SE Spain (Aranda & Molina, 2006; Cámara & Molina, 2009; Hernández Pérez et al., 2016; Lull et al., 2013; Molina, 1978; Risch & Meller, 2015; Schubart et al., 2000). This early
550 abandonment overlaps with the beginning of the seismic cluster recorded in the RUB trench. We hypothesize that the GF seismic crisis could have played a key role, by adding extra stress to the societal crisis and therefore leading to an early abandonment of the settlements. In addition to the occurrence of several earthquakes close in time, their impact on settlements could have been amplified due to the topographic effect (eg., Geli *et al*., 1988) derived from their steep position. Earthquake clusters have also been postulated as triggers to the collapse and destruction of Bronze Age settlements in other regions, such

555 as the Aegean and Eastern Mediterranean (Nur & Cline, 2000) or the Caucasus (Von Suchodoletz et al., 2022b). To further validate this hypothesis, complementary studies are necessary, including dating the more recent archaeological artefacts in the sites (other than tombs) and archaeoseismological analyses.

5 Conclusions

560 The palaeoseismological analysis presented here yields the first seismogenic characterization of the GF. Our results indicate that this active structure ruptured at least 7 or 8 times during the last ca. 24000 yr with a recurrence interval ranging between 1520 and 1720 yr. Our results seem to indicate that the GF is prone to produce earthquake clusters, as we recorded five palaeoseismic events in ca. 400 yr (ca. 1536-1126 BC), and only two events in the next ca. 3200 yr.

We also carried out a seismogenic characterization of the GF using various approaches and scale relationships incorporated

565 into the FiSH code. With this approach, we obtained a maximum expected magnitude for the GF of 6.7 ± 0.3 and a recurrence interval of 1857 yr (CV: 1.2), which is in good agreement with the palaeoseismological results. Furthermore, we followed Okada's approach to estimate the deformation field produced by a maximum earthquake in the GF. This simulation shows that maximum displacement would be experienced in the northern part of the fault, and not in the central sector as expected. This could be related to a fault bend.

570 Finally, the abovementioned earthquake cluster of the GF partially overlaps with the abandonment of two Bronze Age settlements located close to the fault. We postulate that the seismic crisis could have added extra stress to these settlements, leading to an early abandonment.

6 Competing interests

575

The contact author has declared that none of the authors has any competing interests

7 Acknowledgements

We acknowledge the comments of the XXXX reviewers and the Editor XXXX, which significantly improved the quality of this paper. This research was funded by the Spanish Ministry of Science, Innovation and University (research projects
580 PID2021-127967NB-I00 and RTI2018-100737-B-I00), Generalitat Valenciana (Valencian Regional Government, research project AICO2021/196) University of Alicante (research project VIGROB053), and RNM325 research group of Junta de Andalucía. The Institut Cartogràfic Valencià, Agencia Valenciana de Seguridad y Respuesta a las Emergencias (Generalitat

Valenciana), Consorcio Provincial para el Servicio de Prevención y Extinción de Incendios y Salvamento de Alicante, Excelentísimas Diputaciones Provinciales de Alicante y Castellón, and the Ayuntamiento de Almoradí also provided partial funding

585

References

Alfaro, P., Delgado, J., de Galdeano, C. S., Galindo-Zaldívar, J., García-Tortosa, F. J., López-Garrido, A. C., López-Casado, C., Marín-Lechado, C., Gil, A., & Borque, M. J. (2008). The Baza Fault: a major active extensional fault in the central Betic

590   Cordillera (south Spain). International Journal of Earth Sciences : Geologische Rundschau, 97(6), 1353-1365. 10.1007/s00531-007-0213-z

Alfaro, P., Sánchez-Alzola, A., Martin-Rojas, I., García-Tortosa, F. J., Galindo-Zaldívar, J., Avilés, M., Garrido, A. C. L., de Galdeano, C. S., Ruano, P., Martínez-Moreno, F. J., Pedrera, A., Lacy, M. C., Borque, M. J., Medina-Cascales, I., & Gil, A. J. (2021). Geodetic fault slip rates on active faults in the Baza sub-Basin (SE Spain): Insights for seismic hazard assessment.

595   Journal of Geodynamics, 144, 101815. 10.1016/j.jog.2021.101815

Alfaro, P., Gibert, L., Moretti, M., García-Tortosa, F. J., Sanz de Galdeano, C., Galindo-Zaldívar, J., & López-Garrido, Á C. (2010). The significance of giant seismites in the Plio-Pleistocene Baza palaeo-lake (S Spain). Terra Nova (Oxford, England), 22(3), 172-179. 10.1111/j.1365-3121.2010.00930.x

Alfaro, P., Moretti, M., & Soria, J. M. (1997). Soft-sediment deformation structures induced by earthquakes (seismites) in

600   pliocene lacustrine deposits (Guadix-Baza Basin, central Betic Cordillera. Eclogae geologicae Helvetiae, 90(3), 531. doi:10.5169/seals-168193 Retrieved from https://www.e-periodica.ch/digbib/view?pid=egh-001:1997:90::767

ARANDA, G., & MOLINA, F. (2006). WEALTH AND POWER IN THE BRONZE AGE OF THE SOUTH-EAST OF THE IBERIAN PENINSULA: THE FUNERARY RECORD OF CERRO DE LA ENCINA. Oxford Journal of Archaeology, 25(1), 47-59. 10.1111/j.1468-0092.2006.00248.x

605   Barka, A. (1996). Slip distribution along the North Anatolian Fault associated with the large earthquakes of the period 1939 to 1967. Bulletin of the Seismological Society of America, 86(5), 1238-1254. 10.1785/BSSA0860051238

Bronk Ramsey, C. (2009). Bayesian Analysis of Radiocarbon Dates. Radiocarbon, 51(1), 337-360. 10.1017/S0033822200033865

C Sanz de Galdeano, F J García-Tortosa, J A Peláez, P Alfaro, J M Azañón, J Galindo-Zaldívar, C López Casado, A C López

610   Garrido, J Rodríguez-Fernández, & P Ruano. (2012). Main active faults in the Granada and Guadix-Baza Basins (Betic Cordillera)/Principales fallas activas de las Cuencas de Granada y Guadix-Baza (Cordillera Bética). Journal of Iberian Geology, 38(1), 209. https://search.proquest.com/docview/1095127976

Calvache Quesada, M. L., & Viseras, C. (1995). Consecuencias geomorfológicas derivadas de un proceso de captura fluvial. Geogaceta, 18, 93-96. https://explore.openaire.eu/search/publication?articleId=od______1388::e1724b22414bbf788c9fe0362ea73d3c

Cámara Serrano, J. A., & Molina, F. (2009). El análisis de la ideología de emulación. El caso de El Argar. Retrieved from http://hdl.handle.net/10481/14999

Cámara Serrano, J. A., & Molina González, F. R. (2011). Jerarquización social en el mundo Argárico (2000-1300 aC). Retrieved from http://hdl.handle.net/10234/46733

Cámara, J. A., Molina, F., Spanedda, L., & Nájera, T. (2018). Costruzione e perpetuazione delle identità sociali. L'utilizzo del rituale funerario nel sud-est della penisola iberica durante l'età del bronzo antico e medio (2100-1350 cal. A.C. . In V. Nizzo (Ed.), Archeologia e antropologia della morte: 3. Costruzione e decostruzione del Sociale. Atti del 3° Incontro Internazionale di Studi di Antropologia e Archeologia a confronto (pp. 237-262). E.S.S. Editorial Service System.

Castro, J., Martin-Rojas, I., Medina-Cascales, I., García-Tortosa, F. J., Alfaro, P., & Insua-Arévalo, J. M. (2018). Active faulting in the central Betic Cordillera (Spain): Palaeoseismological constraint of the surface-rupturing history of the Baza Fault (Central Betic Cordillera, Iberian Peninsula). Tectonophysics, 736, 15-30. 10.1016/j.tecto.2018.04.010

Castro, P. V. (2001). La sociedad argárica. In M. Gálvez Priego (Ed.), La Edad del Bronce ¿Primera Edad de Oro de España? Sociedad, economía e ideología (pp. 11-21). Crítica.

Chéry, J., Carretier, S., & Ritz, J. (2001). Postseismic stress transfer explains time clustering of large earthquakes in Mongolia. Earth and Planetary Science Letters, 194(1-2), 277-286. 10.1016/S0012-821X(01)00552-0

Corbí, H., Lancis, C., García-García, F., Pina, J., Soria, J. M., Tent-Manclús, J. E., & Viseras, C. (2012). Updating the marine biostratigraphy of the Granada Basin (central Betic Cordillera). Insight for the Late Miocene palaeogeographic evolution of the Atlantic – Mediterranean seaway. Geobios, 45(3), 249-263. 10.1016/j.geobios.2011.10.006

de Galdeano, C. S., & Vera, J. A. (1992). Stratigraphic record and palaeogeographical context of the Neogene basins in the Betic Cordillera, Spain. Basin Research, 4(1), 21-36. 10.1111/j.1365-2117.1992.tb00040.x

DeMets, C., Gordon, R. G., Argus, D. F., & Stein, S. (1994). Effect of recent revisions to the geomagnetic reversal time scale on estimates of current plate motions. Geophysical Research Letters, 21(20), 2191-2194. 10.1029/94GL02118

Diaz-Hernandez, J., & Julia, R. (2006). Geochronological position of badlands and geomorphological patterns in the Guadix–Baza Basin (SE Spain). Quaternary Research, 65(3), 467-477. 10.1016/j.yqres.2006.01.009

DuRoss, C. B., Personius, S. F., Crone, A. J., Olig, S. S., & Lund, W. R. (2011). Integration of paleoseismic data from multiple sites to develop an objective earthquake chronology; application to the Weber Segment of the Wasatch fault zone, Utah. Bulletin of the Seismological Society of America, 101(6), 2765-2781. 10.1785/0120110102

edited by Benny J. Peiser, & Trevor Palmer and Mark E. Bailey. (1998). Natural catastrophes during Bronze Age civilisations : archaeological, geological, astronomical and cultural perspectives : pbk. Hadrian Books [distributor].

Force, E. R. (2017). Seismic Environments of Prehistoric Settlements in Northern Mesopotamia: A Review of Current Knowledge. Bulletin of the American Schools of Oriental Research, 378(378), 55-69. 10.5615/bullamerschoorie.378.0055

Galindo-Zaldívar, J., Jabaloy, A., Serrano, I., Morales, J., González-Lodeiro, F., & Torcal, F. (1999). Recent and present-day stresses in the Granada Basin (Betic Cordilleras): Example of a late Miocene-present-day extensional basin in a convergent plate boundary. Tectonics (Washington, D.C.), 18(4), 686-702. 10.1029/1999TC900016

650 Galindo-Zaldívar, J., González-Lodeiro, F., & Jabaloy, A. (1993). Stress and palaeostress in the Betic-Rif cordilleras (Miocene to the present). Tectonophysics, 227(1), 105-126. https://doi.org/10.1016/0040-1951(93)90090-7

Galindo-Zaldivar, J., Gil, A. J., Sanz de Galdeano, C., Lacy, M. C., García-Armenteros, J. A., Ruano, P., Ruiz, A. M., Martínez-Martos, M., & Alfaro, P. (2015). Active shallow extension in central and eastern Betic Cordillera from CGPS data. Tectonophysics, 663, 290-301. 10.1016/j.tecto.2015.08.035

655 García-Aguilar, J. M., & Martín, J. M. (2000). Late Neogene to recent continental history and evolution of the Guadix-Baza basin (SE Spain). Revista De La Sociedad Geológica De España, 13(1), 65-77.

García-Aguilar, J. M., & Palmqvist, P. (2011). A model of lacustrine sedimentation for the Early Pleistocene deposits of Guadix-Baza basin (southeast Spain). Quaternary International, 243(1), 3-15. 10.1016/j.quaint.2011.02.008

García-Tortosa, F. J., Alfaro, P., Galindo-Zaldívar, J., Gibert, L., López-Garrido, A. C., Sanz de Galdeano, C., & Ureña, M.

660 (2008). Geomorphologic evidence of the active Baza Fault (Betic Cordillera, South Spain). Geomorphology (Amsterdam, Netherlands), 97(3), 374-391. 10.1016/j.geomorph.2007.08.007

García-Tortosa, F. J., Alfaro, P., Sanz de Galdeano, C., & Galindo-Zaldívar, J. (2011). Glacis geometry as a geomorphic marker of recent tectonics: The Guadix–Baza basin (South Spain). Geomorphology (Amsterdam, Netherlands), 125(4), 517-529. 10.1016/j.geomorph.2010.10.021

665 Gibert, L., Alfaro, P., García-Tortosa, F. J., & Scott, G. (2011). Superposed deformed beds produced by single earthquakes (Tecopa Basin, California): Insights into paleoseismology. Sedimentary Geology, 235(3), 148-159. 10.1016/j.sedgeo.2010.08.003

Gibert, L., Scott, G., Martin, R., & Gibert, J. (2007). The Early to Middle Pleistocene boundary in the Baza Basin (Spain). Quaternary Science Reviews, 26(17), 2067-2089. 10.1016/j.quascirev.2007.06.012

670 Gibert, L., Ortí, F., & Rosell, L. (2007). Plio-Pleistocene lacustrine evaporites of the Baza Basin (Betic Chain, SE Spain). Sedimentary Geology, 200(1), 89-116. 10.1016/j.sedgeo.2007.03.003

Gil, A. J., Galindo-Zaldívar, J., Sanz de Galdeano, C., Borque, M. J., Sánchez-Alzola, A., Martinez-Martos, M., & Alfaro, P. (2017). The Padul normal fault activity constrained by GPS data: Brittle extension orthogonal to folding in the central Betic Cordillera. Tectonophysics, 712-713, 64-71. 10.1016/j.tecto.2017.05.008

675 Green, R. A., & Bommer, J. J. (2019). What is the smallest earthquake magnitude that needs to be considered in assessing liquefaction hazard? Earthquake Spectra, 35(3), 1441-1464. 10.1193/032218EQS064M

Hernández Pérez, M. S., Barciela González, V., & García Atiénzar, G. (2016). Cabezo redondo (Primera edición ed.). Universidad de Alicante.

Herraiz, M., De Vicente, G., Lindo-Ñaupari, R., Giner, J., Simón, J. L., González-Casado, J. M., Vadillo, O., Rodríguez-

680 Pascua, M. A., Cicuéndez, J. I., Casas, A., Cabañas, L., Rincón, P., Cortés, A. L., Ramírez, M., & Lucini, M. (2000). The

recent (upper Miocene to Quaternary) and present tectonic stress distributions in the Iberian Peninsula. Tectonics (Washington, D.C.), 19(4), 762-786. 10.1029/2000TC900006

Klinger, Y., Xu Xiwei, X. X., Tapponnier, P., van der Woerd, J., Lasserre, C., & King, G. (2005). High-resolution satellite imagery mapping of the surface rupture and slip distribution of the Mw ~7.8, 14 November 2001 Kokoxili earthquake, Kunlun Fault, Northern Tibet, China. Bulletin of the Seismological Society of America, 95(5), 1970-1987. 10.1785/0120040233

Leonard, M. (2010). Earthquake fault scaling; self-consistent relating of rupture length, width, average displacement, and moment release. Bulletin of the Seismological Society of America, 100(5A), 1971-1988. 10.1785/0120090189

Lozano, L., Cantavella, J. V., Gaite, B., Ruiz-Barajas, S., Antón, R., & Barco, J. (2022). Seismic analysis of the 2020-2021 Santa Fe seismic sequence in the Granada Basin, Spain; relocations and focal mechanisms. Seismological Research Letters, 93(6), 3246-3265. 10.1785/0220220097

Lull, V., Micó, R., Rihuete, C., & Risch, R. (2013). Political collapse and social change at the end of El Argar. In H. Meller, F. Bertemes, H. R. Bork & R. Risch (Eds.), 1600 – Kultureller Umbruch im Schatten des Thera-Ausbruchs? (pp. 283-302). Landesmuseum für vorgeschichte.

Madarieta-Txurruka, A., Galindo-Zaldívar, J., González-Castillo, L., Peláez, J. A., Ruiz-Armenteros, A. M., Henares, J., Garrido-Carretero, M. S., Avilés, M., & Gil, A. J. (2021a). High- and Low-Angle Normal Fault Activity in a Collisional Orogen: The Northeastern Granada Basin (Betic Cordillera). Tectonics (Washington, D.C.), 40(7), n/a. 10.1029/2021TC006715

Madarieta-Txurruka, A., Galindo-Zaldívar, J., González-Castillo, L., Peláez, J. A., Ruiz-Armenteros, A. M., Henares, J., Garrido-Carretero, M. S., Avilés, M., & Gil, A. J. (2021b). High- and Low-Angle Normal Fault Activity in a Collisional Orogen: The Northeastern Granada Basin (Betic Cordillera). Tectonics (Washington, D.C.), 40(7), n/a. 10.1029/2021TC006715

Madarieta-Txurruka, A., González-Castillo, L., Peláez, J. A., Catalán, M., Henares, J., Gil, A. J., Lamas-Fernández, F., & Galindo-Zaldívar, J. (2022). The Role of Faults as Barriers in Confined Seismic Sequences: 2021 Seismicity in the Granada Basin (Betic Cordillera). Tectonics (Washington, D.C.), 41(9), n/a. 10.1029/2022TC007481

Marco, S., Rockwell, T. K., Heimann, A., Frieslander, U., & Agnon, A. (2005). Late Holocene activity of the Dead Sea Transform revealed in 3D palaeoseismic trenches on the Jordan Gorge segment. Earth and Planetary Science Letters, 234(1), 189-205. 10.1016/j.epsl.2005.01.017

Martin-Rojas, I., Alfaro, P., Galindo-Zaldivar, J., Borque-Arancón, M. J., García-Tortosa, F. J., Sanz de Galdeano, C., Avilés, M., Sánchez-Alzola, A., González-Castillo, L., Ruano, P., Medina-Cascales, I., Tendero-Salmerón, V., Madarieta-Txurruka, A., Pedrosa-González, M. T., & Gil-Cruz, A. J. (2023). Insights of Active Extension Within a Collisional Orogen From GNSS (Central Betic Cordillera, S Spain). Tectonics (Washington, D.C.), 42(7), n/a. 10.1029/2022TC007723

Martínez-Martínez, J. M., Booth-Rea, G., Azañón, J. M., & Torcal, F. (2006). Active transfer fault zone linking a segmented extensional system (Betics, southern Spain): Insight into heterogeneous extension driven by edge delamination. Tectonophysics, 422(1), 159-173. 10.1016/j.tecto.2006.06.001

715   Martínez-Solares, J. M., & Mezcua, J. (2002). Catálogo sísmico de la Península Ibérica. Madrid (Spain): Instituto Geográfico Nacional.

Mastrolorenzo, G., Petrone, P., Pappalardo, L., & Sheridan, M. F. (2006). The Avellino 3780-yr-B.P. Catastrophe as a Worst-Case Scenario for a Future Eruption at Vesuvius. Proceedings of the National Academy of Sciences - PNAS, 103(12), 4366-4370. 10.1073/pnas.0508697103

720   Medina-Cascales, I., Martin-Rojas, I., García-Tortosa, F. J., Peláez, J. A., & Alfaro, P. (2020a). Geometry and kinematics of the Baza Fault (central Betic Cordillera, South Spain): insights into its seismic potential. Geologica Acta, 18(1), 1-25. 10.1344/GeologicaActa2020.18.11

Medina-Cascales, I., Martin-Rojas, I., Peláez Montilla, J. A., García Tortosa, F. J., & Alfaro, P. (2020b). Geometry and kinematics of the Baza Fault (central Betic Cordillera, South Spain): insights into its seismic potential. Geologica Acta, 18(1)

725   https://dialnet.unirioja.es/servlet/oaiart?codigo=7689203

Medina-Cascales, I., García-Tortosa, F. J., Martin-Rojas, I., Pérez-Peña, J. V., & Alfaro, P. (2021a). Tectonic geomorphology of an active slow-moving, intrabasinal fault: The Galera Fault (Guadix-Baza Basin, central Betic Cordillera, southern Spain). Geomorphology (Amsterdam, Netherlands), 393, 107941. 10.1016/j.geomorph.2021.107941

Medina-Cascales, I., García-Tortosa, F. J., Martin-Rojas, I., Pérez-Peña, J. V., & Alfaro, P. (2021b). Tectonic geomorphology

730   of an active slow-moving, intrabasinal fault: The Galera Fault (Guadix-Baza Basin, central Betic Cordillera, southern Spain). Geomorphology (Amsterdam, Netherlands), 393, 107941. 10.1016/j.geomorph.2021.107941

Medina-Cascales, I., Koch, L., Cardozo, N., Martin-Rojas, I., Alfaro, P., & García-Tortosa, F. J. (2019). 3D geometry and architecture of a normal fault zone in poorly lithified sediments: A trench study on a strand of the Baza Fault, central Betic Cordillera, south Spain. Journal of Structural Geology, 121, 25-45. 10.1016/j.jsg.2019.02.003

735   MOLINA GONZÁLEZ, F. (1978). Definición y sistematización del Bronce Tardío y Final en el Sudeste de la Península Ibérica. Cuadernos de prehistoria de la Universidad de Granada, 3, 159-232. Retrieved from https://search.proquest.com/docview/1303720145

Molina González, F., Cámara Serrano, J. A., Afonso Marrero, J. A., & Nájera Colino, T. (2014). Las sepulturas del Cerro de la Virgen (Orce, Granada). Diferencias cronológicas y sociales. Revista Atlántica-Mediterránea De Prehistoria Y Arqueología

740   Social, 16, 121-142. 10.25267/Rev_atl-mediterr_prehist_arqueol_soc.2014.v16.13

Molina González, F., Pérez Bareas, C., Spanedda, L., & Cámara Serrano, J. A. (2018). Una nueva lectura de las fortificaciones calcolíticas del Cero de la Virgen (Orce, Granada, España). Ophiussa, 2, 25-37. Retrieved from http://hdl.handle.net/10481/57581

Molina González, F., Cámara Serrano, J. A., Delgado Huertas, A., Jiménez Brobeil, S. A., Nájera Colino, T., Riquelme Cantal,

745   J. A., & Spanedda, L. (2016). Problemas cronológicos y análisis de dieta en la Edad del Bronce de los Altiplanos granadinos: El caso del Cerro de la Virgen (Orce, Granada, España). () Museo de Prehistoria de Valencia. Retrieved from http://hdl.handle.net/10481/48129

Molina González, F., Cámara Serrano, J. A., Dorado Alejos, A., & Villarroya Arín, M. (2017). El fenómeno campaniforme en el Sudeste de la Península Ibérica: el caso del Cerro de la Virgen (Orce, Granada). In V. S. Gonçalves (Ed.), Sinos e Taças.
750   Junto ao Oceano e mais longe. Aspectos da presença campaniforme na Península Ibérica (pp. 258-275). Lisboa: Universidade do Lisboa. Retrieved from http://hdl.handle.net/10481/49777

Molina González, F., Pérez Bareas, C., Spanedda, L., & Cámara Serrano, J. A. (2018). Una nueva lectura de las fortificaciones calcolíticas del Cero de la Virgen (Orce, Granada, España). Retrieved from http://hdl.handle.net/10481/57581

Molina, F. (1983). La Prehistoria. In F. Molina, & J. M. Roldán (Eds.), Historia de Granada I. De las primeras culturas al Islam
755   (pp. 11-131). Don Quijote.

Molina, F., & Cámara, J. A. (2004). La Cultura del Argar en el área occidental del Sudeste. In L. Hernández, & M. S. Hernández (Eds.), La Edad del Bronce en tierras valencianas y zonas limítrofes (pp. 455-470). Ayuntamiento de Villena/Instituto Alicantino de Cultura Juan Gil-Albert.

Morales, J., Serrano, I., Vidal, F., & Torcal, F. (1997). The depth of the earthquake activity in the Central Betics (Southern
760   Spain). Geophysical Research Letters, 24(24), 3289-3292. 10.1029/97GL03306

Moretti, M., Alfaro, P., Caselles, O., & Canas, J. A. (1999). Modelling seismites with a digital shaking table. Tectonophysics, 304(4), 369-383. 10.1016/S0040-1951(98)00289-3

MUNOZ, A., & UDIAS, A. (1991). Three large historical earthquakes in Southern Spain.(8), 175-182.

Nocquet, J. (2012). Present-day kinematics of the Mediterranean: A comprehensive overview of GPS results. Tectonophysics,
765   579, 220-242. 10.1016/j.tecto.2012.03.037

Nur, A., & Cline, E. H. (2000). Poseidon's Horses: Plate Tectonics and Earthquake Storms in the Late Bronze Age Aegean and Eastern Mediterranean. Journal of Archaeological Science, 27(1), 43-63. 10.1006/jasc.1999.0431

Okada, Y. (1985). Surface deformation due to shear and tensile faults in a half-space. Bulletin of the Seismological Society of America, 75(4), 1135-1154. 10.1785/BSSA0750041135

770   Okada, Y. (1992). Internal deformation due to shear and tensile faults in a half-space. Bulletin of the Seismological Society of America, 82(2), 1018-1040. 10.1785/BSSA0820021018

Oswald, P., Strasser, M., Hammerl, C., & Moernaut, J. (2021). Seismic control of large prehistoric rockslides in the Eastern Alps. Nature Communications, 12(1), 1059. 10.1038/s41467-021-21327-9

Owen, G. (1987). Deformation processes in unconsolidated sands

775   P.V. Castro Martínez, R.W. Chapman, S. Gili Suriñach, V. Lull, R. Micó Pérez, C. Rihuete Herrada, R. Risch, & Mª E. Sanahuja Yll. (2009). TIEMPOS SOCIALES DE LOS CONTEXTOS FUNERARIOS ARGÁRICOS|TIEMPOS SOCIALES DE LOS CONTEXTOS FUNERARIOS ARGÁRICOS. Anales De Prehistoria Y Arqueología, (9-10) http://revistas.um.es/index.php/apa/article/view/64001

Pace, B., Visini, F., & Peruzza, L. (2016). FiSH; MATLAB tools to turn fault data into seismic-hazard models. Seismological
780   Research Letters, 87(2A), 374-386. 10.1785/0220150189

Pedrera, A., Marin-Lechado, C., Galindo-Zaldivar, J., Rodriguez-Fernandez, L. R., & Ruiz-Constan, A. (2006). Fault and fold interaction during the development of the Neogene-Quaternary Almeria-Nijar basin (SE Betic Cordilleras). Geological Society Special Publication, 262(1), 217-230. 10.1144/GSL.SP.2006.262.01.13

Peña, J. A. (1985). La depresión de Guadix-Baza | La depresión de Guadix-Baza. Estudios Geológicos, 41(1-2), 33-46. Retrieved from http://estudiosgeol.revistas.csic.es/index.php/estudiosgeol/article/view/688

Pérez-Peña, A., Martín-Davila, J., Gárate, J., Berrocoso, M., & Buforn, E. (2010). Velocity field and tectonic strain in Southern Spain and surrounding areas derived from GPS episodic measurements. Journal of Geodynamics, 49(3), 232-240. 10.1016/j.jog.2010.01.015

Ramsey, C. B. (2008). Deposition models for chronological records. Quaternary Science Reviews, 27(1), 42-60. 10.1016/j.quascirev.2007.01.019

Reicherter, K., Jabaloy, A., Galindo-Zaldívar, J., Ruano, P., Becker-Heidmann, P., Morales, J., Reiss, S., & González-Lodeiro, F. (2003). Repeated palaeoseismic activity of the Ventas de Zafarraya fault (S Spain) and its relation with the 1884 Andalusian earthquake. International Journal of Earth Sciences : Geologische Rundschau, 92(6), 912-922. 10.1007/s00531-003-0366-3

Reimer, P. J., Austin, W. E. N., Bard, E., Bayliss, A., Blackwell, P. G., Bronk Ramsey, C., Butzin, M., Cheng, H., Edwards, R. L., Friedrich, M., Grootes, P. M., Guilderson, T. P., Hajdas, I., Heaton, T. J., Hogg, A. G., Hughen, K. A., Kromer, B., Manning, S. W., Muscheler, R., . . . Talamo, S. (2020). The IntCal20 Northern Hemisphere Radiocarbon Age Calibration Curve (0–55 cal kBP). Radiocarbon, 62(4), 725-757. 10.1017/RDC.2020.41

Risch, R., & Meller, H. (2015). Change and Continuity in Europe and the Mediterranean around 1600 bc. Proceedings of the Prehistoric Society, 81, 239-264. 10.1017/ppr.2015.10

Rockwell, T. K., Dawson, T. E., Young Ben-Horin, J., & Seitz, G. (2015). A 21-Event, 4,000-Year History of Surface Ruptures in the Anza Seismic Gap, San Jacinto Fault, and Implications for Long-term Earthquake Production on a Major Plate Boundary Fault. Pure and Applied Geophysics, 172(5), 1143-1165. 10.1007/s00024-014-0955-z

Rodriguez-Fernandez, J., & Sanz de Galdeano, C. (2006). Late orogenic intramontane basin development: the Granada basin, Betics (southern Spain). Basin Research, 18(1), 85-102. 10.1111/j.1365-2117.2006.00284.x

Ruano, P., Galindo-Zaldívar, J., & Jabaloy, A. (2004). Recent Tectonic Structures in a Transect of the Central Betic Cordillera. Pure and Applied Geophysics, 161(3), 541-563. 10.1007/s00024-003-2462-5

Sanz de Galdeano, C., & Alfaro, P. (2004). Tectonic significance of the present relief of the Betic Cordillera. Geomorphology (Amsterdam, Netherlands), 63(3), 175-190. 10.1016/j.geomorph.2004.04.002

Sanz de Galdeano, C., Peláez Montilla, J. A., & López Casado, C. (2003). Seismic Potential of the Main Active Faults in the Granada Basin (Southern Spain). Pure and Applied Geophysics, 160(8), 1537-1556. 10.1007/s00024-003-2359-3

Sanz de Galdeano, C., Azañón, J. M., Cabral, J., Ruano, P., Alfaro, P., Canora, C., Ferrater, M., García Tortosa, F. J., García-Mayordomo, J., Gràcia, E., Insua-Arévalo, J. M., Jiménez Bonilla, A., Lacan, P. G., Marín-Lechado, C., Martín-Banda, R., Martín González, F., Martínez-Díaz, J. J., Martín-Rojas, I., Masana, E., . . . Simón, J. L. (2020). Active Faults in Iberia. In C.

Quesada, & J. T. Oliveira (Eds.), The Geology of Iberia: A Geodynamic Approach: Volume 5: Active Processes: Seismicity,
815   Active Faulting and Relief (pp. 33-75). Springer International Publishing. 10.1007/978-3-030-10931-8_4

Schubart, H., Pingel, V., & Arteaga, O. (2000). Fuente Álamo. Las excavaciones arqueológicas 1977-1991 en el poblado de
la Edad de Bronce. Junta de Andalucía. 2000. Junta de Andalucía.

Schüle, W. (1980). Orce und Galera. Zwei Siedlungen aus dem 3. bis 1. Jahrtausend v. Chr. im Südosten der Iberischen
Halbinsel. I. Übersicht über die Ausgrabungen 1962-1970 (Book Review). Basel: Schwabe & Co. Retrieved from
820   https://search.proquest.com/docview/1308882337

SCOTT, G. R., & GIBERT, L. (2009). The oldest hand-axes in Europe. Nature (London), 461(7260), 82-85.
10.1038/nature08214

Serpelloni, E., Vannucci, G., Pondrelli, S., Argnani, A., Casula, G., Anzidei, M., Baldi, P., & Gasperini, P. (2007). Kinematics
of the Western Africa-Eurasia plate boundary from focal mechanisms and GPS data. Geophysical Journal International, 169(3),
825   1180-1200. 10.1111/j.1365-246X.2007.03367.x

Silva Barroso, P. G., Rodríguez Pascua, M. A., Giner Robles, J. L., Pérez López, R., Lario Gómez, J., Perucha Atienza, M. A.,
Bardají Azcárate, T., Huerta Hurtado, P., Roquero García- Casal, E., & Bautista Davila, M. B. (2014). Catálogo de los efectos
geológicos de los

terremotos en España. IGME, AEQUA.

830   Sims, J. D. (1975). Determining earthquake recurrence intervals from deformational structures in young lacustrine sediments.
Tectonophysics, 29(1), 141-152. 10.1016/0040-1951(75)90139-0

SORIA, F. J., LOPEZ-GARRIDO, A. C., & VERA, J. A. (1987). Análisis estratigráfico y sedimentológico de los depositos
neógeno-cuaternarios en el sector de Orce, depresión de Guadix-Baza. Paleontol. evol. Mem. esp., (1), 11-34.

Soria, J. M., Fernández, J., & Viseras, C. (1999). Late Miocene stratigraphy and palaeogeographic evolution of the
835   intramontane Guadix Basin (Central Betic Cordillera, Spain): implications for an Atlantic–Mediterranean connection.
Palaeogeography, Palaeoclimatology, Palaeoecology, 151(4), 255-266. 10.1016/S0031-0182(99)00019-X

Toda, S., Stein, R., Sevilgen, V., & Lin, J. (2011). Coulomb 3.3 Graphic-rich deformation and stress-change software for
earthquake, tectonic, and volcano research and teaching-user guide. (). Retrieved from Aquatic Science & Fisheries Abstracts
(ASFA) Professional https://search.proquest.com/docview/907169304

840   Tuttle, M., Hartleb, R., Wolf, L., & Mayne, P. (2019). Paleoliquefaction Studies and the Evaluation of Seismic Hazard.
Geosciences, 9(7), 311. 10.3390/geosciences9070311

Vera, J. A. (1970). Estudio estratigráfico de la Depresión de Guadix-Baza. Boletín Geológico Y Minero, 81, 429-462.

VERA, J. A., FERNANDEZ, J., LOPEZ-GARRIDO, A. C., & RODRIGUEZ-FERNANDEZ, J. (1983). Geologìa y
estratigrafìa de los materìales plioceno-pleistoceno del sector Orde-Venta Micena, Prov. Granada. Paleontol. Evol., 18, 3-11.

845   Von Suchodoletz, H., Kirkitadze, G., Koff, T., Fischer, M. L., Poch, R. M., Khosravichenar, A., Schneider, B., Glaser, B.,
Lindauer, S., Hoth, S., Skokan, A., Navrozashvili, L., Lobjanidze, M., Akhalaia, M., Losaberidze, L., & Elashvili, M. (2022a).

Human-environmental interactions and seismic activity in a Late Bronze to Early Iron Age settlement center in the southeastern Caucasus. Frontiers in Earth Science (Lausanne), 1010.3389/feart.2022.964188

Von Suchodoletz, H., Kirkitadze, G., Koff, T., Fischer, M. L., Poch, R. M., Khosravichenar, A., Schneider, B., Glaser, B.,
850 Lindauer, S., Hoth, S., Skokan, A., Navrozashvili, L., Lobjanidze, M., Akhalaia, M., Losaberidze, L., & Elashvili, M. (2022b). Human-environmental interactions and seismic activity in a Late Bronze to Early Iron Age settlement center in the southeastern Caucasus. Frontiers in Earth Science (Lausanne), 1010.3389/feart.2022.964188

Walker, J., Gaffney, V., Fitch, S., Muru, M., Fraser, A., Bates, M., & Bates, R. (2020). A great wave: the Storegga tsunami and the end of Doggerland? Antiquity, 94(378), 1409-1425. 10.15184/aqy.2020.49

855 Wells, D. L., & Coppersmith, K. J. (1994). New empirical relationships among magnitude, rupture length, rupture width, rupture area, and surface displacement. Bulletin of the Seismological Society of America, 84(4), 974-1002. https://pubs.geoscienceworld.org/ssa/bssa/article/84/4/974/119792